THESIS FOR THE DEGREE OF LICENTIATE OF ENGINEERING

Materials for proton exchange membrane fuel cells and electrolyzers

Combining SEM imaging, Raman spectroscopy and other experimental methods

Dylan Schulz

CHALMERS

Department of Chemistry and Chemical Engineering
CHALMERS UNIVERSITY OF TECHNOLOGY
Göteborg, Sweden 2026

Materials for proton exchange membrane fuel cells and electrolyzers

Combining SEM imaging, Raman spectroscopy and other experimental methods

Dylan Schulz

Licentiatuppsatser vid Institutionen för kemi och kemiteknik
Chalmers tekniska högskola
Nr 2026:13

Department of Chemistry and Chemical Engineering
Chalmers University of Technology
SE-412 96 Göteborg
Telephone +46 31 772 1000

Cover:
An illustration of scanning electron microscope and Raman microscope data being collected from a gas diffusion layer sample.

Printed by Chalmers digitaltryck
Göteborg, Sweden 2026

"Yes, my friends, I believe that water will one day be employed as fuel, that hydrogen and oxygen which constitute it, used singly or together, will furnish an inexhaustible source of heat and light, of an intensity of which coal is not capable."

— Jules Verne, *The Mysterious Island*, 1874

Materials for proton exchange membrane fuel cells and electrolyzers
Combining SEM imaging, Raman spectroscopy and other experimental methods

Dylan Schulz
Department of Chemistry and Chemical Engineering
Chalmers University of Technology

Abstract

The global transition toward a decarbonized energy infrastructure requires robust energy storage solutions to balance intermittent renewable power. When paired, polymer electrolyte membrane (PEM) electrolyzers and fuel cells offer an effective mechanism for the generation, and utilization of green hydrogen. However, optimizing these devices requires a profound understanding of their complex, multi-phase porous transport media. A persistent challenge in materials science is decoupling the intricate chemical and structural interactions within these components on a micro-scale.

In this work, identical location (IL) methodologies are developed and applied to bridge the gap between macroscopic electrochemical performance and localized microscopic phenomena. By coupling scanning electron microscopy (SEM) with chemical spectroscopy (EDX and confocal Raman) and tracking identical material locations before assembly and after disassembly, individual component behaviors can be isolated. For fuel cell gas diffusion layers (GDLs), co-located Raman mapping and SEM/EDX imaging shows that the base carbon architecture and presence of a binder substantially controls the spatial distribution of hydrophobic polymer treatments in the studied samples. For electrolyzer porous transport electrodes (PTEs), IL imaging verifies the mechanical survivability of novel, high-surface-area platinized carbon nanofiber scaffolds even after extended operation. Furthermore, Raman analysis of the imprints left by such rigid PTEs on the proton exchange membrane (PEM) highlights how non-uniform interfacial contact drives localized chemical degradation. This thesis seeks to combine such methods to provide a better understanding of the materials and interfaces in PEM fuel cells and electrolyzers.

Keywords: Fuel Cells, Electrolyzers, Proton Exchange Membranes, Identical location, Raman spectroscopy, SEM, EDX

List of Publications

This thesis is based on the following appended papers, referred to by Roman numerals in the text:

I. The Role of Native Binder in Controlling the Polytetrafluoroethylene Distribution in Gas Diffusion Layers for Proton Exchange Membrane Fuel Cells

D. Schulz, M. Ringström, S. Sankar and A. Martinelli

Accepted in Fuel Cells, 2026

II. Robust anodes for PEM electrolysers based on platinized carbon nanofibers with low iridium loading

D. Schulz, X. Wen, B. Penninckx, S. Sasidharan, L. Strandberg, F. Wenger and A. Martinelli

In manuscript

My Contributions to the Publications

Paper I

I performed all Raman, SEM and EDX measurements and assisted in the analysis of the limiting current experiments. I prepared the initial draft of the manuscript and finalized the manuscript together with the co-authors.

Paper II

I performed the Raman and SEM experiments, made the FIB cuts and assisted with some of the TEM characterizations. I performed the imprint analysis and wrote the manuscript draft.

Acknowledgments

Before beginning this thesis, I would like to offer my gratitude to the many wonderful people who have supported me on this journey.

First of all, I would like to thank the Swedish Electricity Storage and Balancing Center for their financial support and the many opportunities to collaborate with other members in the center.

I would like express my sincerest gratitude to Anna Martinelli for all her help and her guidance, and for alaways being patient no matter what crazy ideas I bring to her. I could not ask for a better supervisor.

I am likewise grateful to my examiner, Magnus Skoglundh, my co-supervisor Anders Palmqvist and my director of studies Ergang Wang for their ongoing support and contributions.

I would like to express my great thanks for my collaborators at Smoltek Hydrogen, Fabian, Sankar, Linnea, Xin and Bastien. You have been a pleasure to work with and I hope for many more engaging scientific conversations with you all.

A big thank you goes to all of my colleagues for the wonderful working environment here at Chalmers. In particular, I would like to thank my office mates Arma and Anna, as well as Vasiliki, Savitha, Andreas, Markus, Jesper and Maria, for bringing such life and joy to Chalmers. There is never a boring day here with all of you around.

A special thank you goes to my mom, Judi, and my brother, Vincent, for your love, care and support. And finally, I wish to thank my dad, Jomi, for inspiring me towards science all my life. I wish you were here to read this.

Dylan Schulz, Göteborg, September 2026

Contents

Abstract iv

List of Publications vii

1 Introduction 1
1.1 Scope of the thesis . . . 2

2 Hydrogen technologies 3
2.1 Why hydrogen? . . . 3
2.1.1 Hydrogen in an energy grid . . . 3
2.1.2 Hydrogen demand and sources . . . 4
2.2 Fuel cell and electrolyzer technologies . . . 5
2.3 Electrochemistry of PEM devices . . . 6
2.3.1 Catalysis . . . 7
2.4 PEM fuel cell and electrolyzer components . . . 9
2.4.1 Proton exchange membranes . . . 9
2.4.2 HER/HOR electrodes . . . 10
2.4.3 ORR/OER electrodes . . . 10
2.4.4 Gas diffusion and porous transport layers . . . 11
2.4.5 Bipolar plates (BPP) . . . 12
2.5 Operations and economics of fuel cells and electrolyzers . . . 12
2.6 Durability . . . 13

3 Methods 15
3.1 Confocal Raman spectroscopy . . . 15
3.2 Electron microscopy . . . 15
3.3 Identical location methods . . . 17
3.4 Electrochemical characterization . . . 18
3.5 Gas physisorption surface area analysis . . . 20
3.6 Sample preparation . . . 21
3.6.1 Gas diffusion layers . . . 21
3.6.2 Carbon nanofiber porous transport electrodes . . . 22

4 Results Summary and Discussion 23
4.1 Paper I: fuel cell gas diffusion layers . . . 23
4.2 Paper II: carbon nanofiber electrolyzer anodes . . . 25

5 Conclusions 27
5.1 Ideas for future work . . . 28
5.2 Closing thoughts and the future of hydrogen . . . 29

Bibliography 31

List of Figures

1.1 Levelized cost of energy (LCOE) for a kilowatt generated by various renewable energy sources. Onshore wind (blue) and solar photovoltaics (green) are now cheaper than all fossil sources. Data source: Our World in Data [11]. . . . 1
1.2 Schematic of a hydrogen economy. . . . 2
1.3 Schematic of a PEM fuel cell and a PEM electrolyzer. . . . 2

2.1 Gravimetric vs volumetric energy density of various fuels, adapted from [21]. The energy density of three main forms of hydrogen storage are circled. . . . 3
2.2 Electricity generation and demand in Sweden's SE3 grid in the week of June 15 - 21 2026. High fluctuations occur due to both changing demand and variable renewable energy sources. Data source: ENTSOE [23]. . . . 4
2.3 Industrial hydrogen production by source technology and hydrogen demand by industrial sector from 2020 to 2024. Data source: IEA [14]. 4
2.4 Example polarization curve for a PEM fuel cell with the regions dominated by activation losses, ohmic losses and mass transport losses marked. . . . 6
2.5 Free energy profile of the catalyzed OER reaction by the adsorbate evolution mechanism (AEM). The reaction steps (equations 2.8a-d) are referenced from [31]. . . . 7
2.6 Sabatier volcano plot showing trends in the ORR activity as a function of the oxygen binding energy for various electrocatalysts. Data source: [33]. . . . 8
2.7 General membrane-electrode assembly (MEA) schematic with bipolar plates. . . . 9
2.8 a) Chemical structure of Nafion, the most common PFSA ionomer. b) Model of the proton-conducting cluster networks in a hydrated proton exchange membrane. The $-SO_3^-$ active groups are marked in red. Data source: [36, 37]. . . . 10
2.9 Illustration of a typical fuel cell electrode composed of platinum nanoparticles on a carbon support bound together with an ionomer. 11
2.10 Layers in a PTE. . . . 11
2.11 a): Component cost breakdown of the stack cost distribution within as 80 kW automotive PEM fuel cell system, data source: [46]. b): Component cost breakdown of a representative 1 MW PEM WE installation, data source: [45]. Note that the methodologies of the two sources are not the same, so only a qualitative comparison is possible. . . . 13

3.1 Energy level diagram illustrating Rayleigh scattering alongside Stokes and anti-Stokes Raman scattering. Note that anti-Stokes scattering requires a significant population of electrons to be in the ν_1 vibrational state, which occurs at high temperatures. . . . 15

3.2 Schematic illustration of a scanning electron microscope. 16
3.3 Interaction volumes in a sample for secondary electrons (SE), backscattered electrons (BSE), and characteristic X-rays (EDX) [52]. 16
3.4 Electronic shell transition diagram for EDX, showing the emission of characteristic K_α and K_β X-ray photons. 17
3.5 Sequential images demonstrating the process of zooming in on an identically located spot on an SEM sample. 18
3.6 Schematic of a standard ex-situ three-electrode electrochemical cell. . 18
3.7 Typical a) fuel cell and b) electrolyzer polarization curves illustrating the activation, ohmic, and mass transport loss regions. 19
3.8 Drawing of the total oxygen transport resistance as a function of absolute pressure, illustrating the deconvolution of R_{P} and R_{NP}. . . . 19
3.9 A standard Tafel plot (η vs. $\log i$) used to extract the Tafel slope and exchange current density. 20
3.10 A representative Nyquist plot for an EIS experiment, showing typical ohmic, charge-transfer and mass-transport impedance features. . . . 20
3.11 Diagram illustrating adsorption and desorption isotherms for a porous material, with the valid range for applying the BET theory shaded. . 21

4.1 Typical spectrum from a Raman mapping experiment. The spectrum shows the D and G carbon C-C vibrational modes and the PTFE C-F stretching mode. 23
4.2 Identical location Raman mapping and SEM/EDX imaging of the wet-laid F-H23 (left) and dry-laid SGL-39AA (right) GDLs. 24
4.3 A representative bar graph for the pressure-dependent part of the (dry) oxygen transport resistance of each of the two GDL types, analyzed at at 200 kPa absolute pressure and 2 % O_2. 24
4.4 Identical location SEM imaging of a PTE section before assembly (top) and after disassembly (bottom). 25
4.5 A PTE electrode grain (top) alongside its corresponding physical imprint left in the polymer membrane (bottom). 25
4.6 Raman spectra of the end-of-life membrane's imprinted and channel regions, normalized to the peak height of the C-F backbone signal. . 26
4.7 The *in-situ* durability test ($2\,\mathrm{A/cm^2}$, $60\,^\circ\mathrm{C}$, atmospheric pressure) utilizing a $0.2\,\mathrm{mg_{Ir}/cm^2}$ catalyst loading on a $5\,\mathrm{cm^2}$ cell area. 26

List of Tables

2.1 Comparison of fuel cell technologies [16, 27, 28]. 5
2.2 Comparison of water electrolyzer technologies [29, 30]. 5

1 Introduction

The last 100 years have seen an enormous and unprecedented increase in human productivity, well-being and population which has done an enormous amount of good for our species.[1] At the same time, the United Nations expects the global population to stabilize around 10.3 billion people by the end of the century [4]. This is excellent news for our species, but has been driven by the extensive use of fossil fuels.

1: For example, the average global life expectancy has increased from 32 years in 1900 to 73 years in 2023 [3].

That scale of fossil fuel usage is problematic as it is the primary driver behind climate change, one of the greatest challenges currently facing our species. In economic terms, a continuation of current warming trends suggests a Social Cost of Carbon in excess of $1,200 per ton [5]. It is imperative to address climate change now because addressing it later will invite greater costs - mitigation now is cheaper, more effective and will lead to a greatly diminished loss of life from climate related disasters [6]. Besides the need to mitigate climate change, we have a strategic imperative to conserve petroleum resources because many processes (especially plastics, oils and lubricants) require fossil feedstocks that are not easily replicable with other means. Simply burning fossil fuels is in many ways shortsighted [7, 8].

Clearly, current fossil fuel consumption for energy use is unsustainable and we further require more energy as global development continues. Thus, we must redesign our energy systems so that energy remains available in high abundance with only limited use of fossil energy sources. Towards this end, we need the mass electrification of industry, transport and heating sectors, which will see global electricity demand increase by ca. 50 % over the next 5 years [9, 10].

Large scale electrification requires a larger share of renewable energies. Wind and solar power in particular are attractive because over the last decade they have become the most economical available power sources (see Figure 1.1) [12]. Wind and solar systems are variable renewable energies whose output is dependent on factors such as the weather and therefore cannot be scaled to demand. An energy grid with a large share of wind and solar power therefore requires energy storage solutions to buffer around energy supply and demand mismatches. For grid balancing on a moment-to-moment timescale, supercapacitors are preferred. For longer timescales, the three most attractive options are pumped hydropower, large scale batteries, and hydrogen technologies [13].

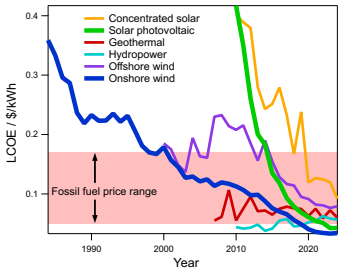

Figure 1.1: Levelized cost of energy (LCOE) for a kilowatt generated by various renewable energy sources. Onshore wind (blue) and solar photovoltaics (green) are now cheaper than all fossil sources. Data source: Our World in Data [11].

This thesis will focus around hydrogen technologies, specifically the proton exchange membrane (PEM) fuel cell and electrolyzer. A PEM electrolyzer can produce hydrogen by electrically splitting water, and a fuel cell does the reverse, using that hydrogen to

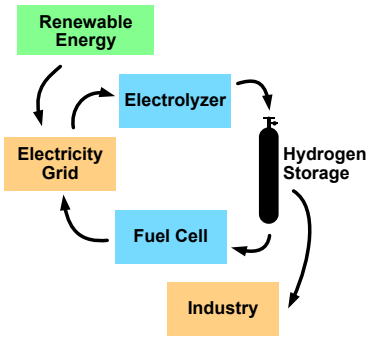

Figure 1.2: Schematic of a hydrogen economy.

generate electricity. Combined, these technologies have the potential to act as energy storage for an electricity grid, converting electricity to hydrogen and hydrogen to electricity as supply and demand require (Figure 1.2). Such a system could also supply hydrogen to industry. The development of hydrogen technology is also vital because the industrial requirement for hydrogen, which was around 100 million tonnes in 2024, is currently dominated by fossil sources [14]. There is consequently a need for large amounts of green hydrogen to supply these industries, as well as other industries which may decarbonize more easily if hydrogen can be supplied cleanly and cheaply [15].

The core concepts of the PEM fuel cell and electrolyzer are equivalent (Figure 1.3). A membrane which is conductive to protons yet electrically insulating separates two half cells, in one of which hydrogen is catalytically split or developed while in the other oxygen is developed or split to form water.[2] The greatest challenges come from the three-phase boundary, which is the need to provide access to a gas phase, an electrically conductive solid phase, and a proton conducting wet phase which leads to the membrane. These three phases need to be brought within a few micrometers of each other for the reaction to take place without undue losses. At the same time, water management is critical, as too much water will flood the cell preventing gas transport and too little water will dry out the cell, preventing the function of the proton conductive membrane and starving reactants in an electrolyzer [16].

2: I will refer to electrodes in this thesis by the reaction which takes place there, eg. OER electrode. This is to avoid confusion with the nomenclature of cathode and anode, which are defined by their electrical potential not the reaction they facilitate. For example, the oxygen half reaction occurs on the anode in an electrolyzer and the cathode in a fuel cell, which causes ambiguity I wish to avoid.

1.1 Scope of the thesis

This thesis seeks to explore how different portions of the membrane-electrode assembly function together in PEM fuel cells and electrolyzers. A major focus is on identical location imaging techniques and Raman spectroscopy, alongside electrochemical results in order to relate the structure, chemistry and performance of PEM fuel cells and electrolyzers.

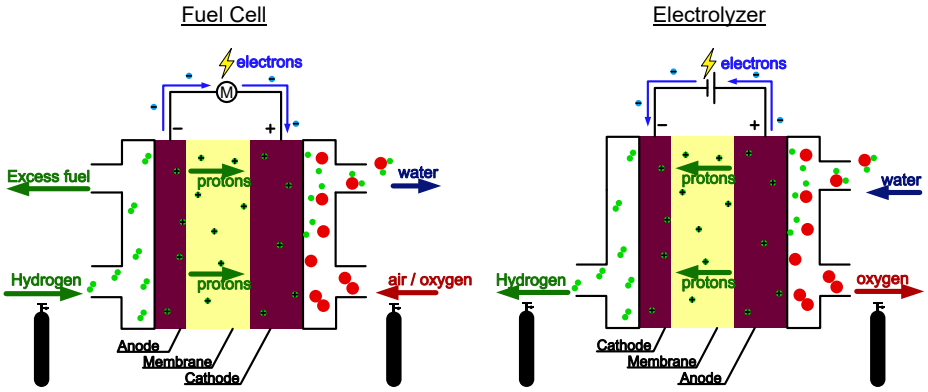

Figure 1.3: Schematic of a PEM fuel cell and a PEM electrolyzer.

Hydrogen technologies 2

Hydrogen is the most abundant element in the universe and has been the subject of many historical scientific milestones. For example, hydrogen was instrumental to early flight systems as a lift gas for balloons and zeppelins [17], the fixation of ammonia by the Haber-Bosch process [18] which to this day remains the largest demand source for hydrogen, and the fuel cells that powered the Apollo lunar missions [19]. For centuries, scientists and researchers have seen an enormous amount of potential in hydrogen, so how can fuel cells and electrolyzers help us to tap into that potential?

2.1 Why hydrogen? 3
2.1.1 Hydrogen in an energy grid 3
2.1.2 Hydrogen demand and sources 4
2.2 Fuel cell and electrolyzer technologies . . . 5
2.3 Electrochemistry of PEM devices 6
2.3.1 Catalysis 7
2.4 PEM fuel cell and electrolyzer components . 9
2.4.1 Proton exchange membranes 9
2.4.2 HER/HOR electrodes 10
2.4.3 ORR/OER electrodes . 10
2.4.4 Gas diffusion and porous transport layers 11
2.4.5 Bipolar plates (BPP) . . 12
2.5 Operations and economics of fuel cells and electrolyzers . . . 12
2.6 Durability 13

2.1 Why hydrogen?

Hydrogen has enormous potential because it is a very available element, is chemically well behaved, and its reactions are clean. Since it can be split from water, it can be produced in principle almost anywhere, and transported in a similar manner to liquefied natural gas [20]. It is also very light, giving hydrogen a far greater gravimetric energy density than any other available fuel sources, though the volumetric energy density is relatively low (Figure 2.1). This makes it an excellent fuel source for any applications where weight is critical, including historically the Apollo missions. For an electrical grid system, hydrogen is attractive because when produced by electrolysis it can act as energy storage in much the same way as a battery of indefinite capacity. Hydrogen could buffer the variable load of renewable energy sources like wind and solar power, though only if it is produced from renewable sources.

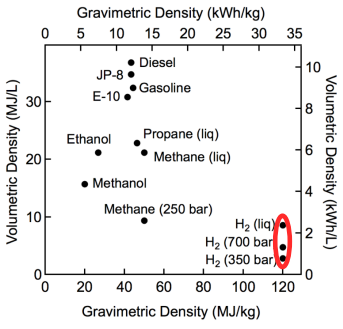

Figure 2.1: Gravimetric vs volumetric energy density of various fuels, adapted from [21]. The energy density of three main forms of hydrogen storage are circled.

2.1.1 Hydrogen in an energy grid

The transition to a low-carbon energy system relies heavily on the integration of Variable Renewable Energy (VRE) sources, predominantly wind and solar power. These power sources can fluctuate significantly, requiring a 'buffer' storage to maintain a balance in an electrical grid. The electrical grid is an energy transmission system, with very little storage capacity [22]. To maintain grid stability, electrical grids must constantly match power generation with power consumption, which may also vary (Figure 2.2). As the amount of VRE in a grid increases, the grid requires more balancing mechanisms to maintain stability. Currently, such balancing services are offered by hydroelectric storage, which is geographically limited and so difficult to expand to the degree needed for

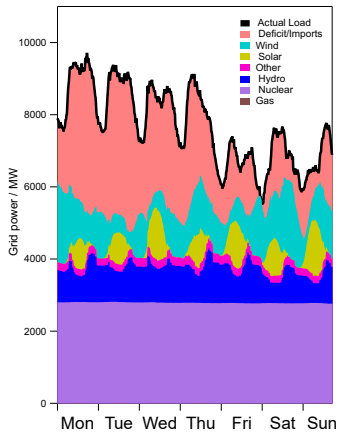

Figure 2.2: Electricity generation and demand in Sweden's SE3 grid in the week of June 15 - 21 2026. High fluctuations occur due to both changing demand and variable renewable energy sources. Data source: ENTSOE [23].

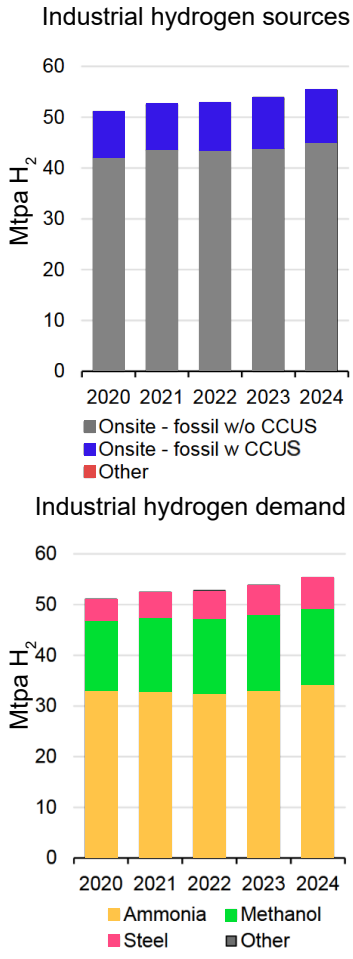

Figure 2.3: Industrial hydrogen production by source technology and hydrogen demand by industrial sector from 2020 to 2024. Data source: IEA [14].

VREs, and gas turbines which are expensive and fossil fuel driven [10].

Hydrogen technologies can act on both the demand (load) side and the supply (generation) side of the grid. On the demand side, electrolyzers can be operated flexibly, changing the amount of electricity they use depending on the grid state, preferentially producing hydrogen when supply is greater than demand. On the supply side, hydrogen fuel cells can consume stored hydrogen to supply electricity back to the grid, smoothing out the intermittent nature of VREs [24].

An advantage of utilizing hydrogen for grid energy storage is the decoupling of power capacity from energy storage capacity. In conventional battery-based storage, power output and energy storage capacity are connected and cannot be independently scaled. In a hydrogen-based storage system, the power capacity is dictated by the capacity of installed fuel cells and electrolyzers, while the energy storage capacity is determined by the size of the storage vessels which can be built independently. This adds significant versatility to hydrogen as a grid balancing medium [24].

2.1.2 Hydrogen demand and sources

The industrial production of hydrogen has historically occurred by coal gasification combined with the water-gas shift reaction,* or from steam reforming of methane† [25], both of which are reliant on fossil fuel sources. Electrolysis could allow us to produce hydrogen from electrical energy, which can be produced renewably from sources like wind and solar [12]. This would make electrical energy from hydrogen fuel cells renewable as well.

Because of the vast differences in the renewability of hydrogen depending on the production method, a color-based classification exists: black or grey hydrogen which is produced from fossil sources, blue hydrogen which is coupled with carbon capture and storage, and green hydrogen which is produced electrolytically from renewable energy sources [26]. Currently, most industrial hydrogen is produced from steam reforming of methane without subsequent carbon capture, i.e. grey hydrogen. The amount of hydrogen produced by industry is very high, exceeding 50 Mtpa, which is mostly used in the synthesis of ammonia and methanol (Figure 2.3).

Clearly a high demand for hydrogen exists from chemical industry. This is a good thing for green hydrogen: in principle, a market

* $$CO + H_2O \rightleftharpoons CO_2 + H_2 \quad (2.1)$$

† $$CH_4 + H_2O \rightleftharpoons CO + 3H_2 \quad (2.2)$$

and basic infrastructure is already in place. However, it also informs the near-to-mid term challenges around hydrogen. Rather than building fuel cell infrastructures to take advantage of green hydrogen, electrolysis should be the more important concern. Fuel cells cannot run without hydrogen, after all, and what hydrogen is currently used must be substantially decarbonized. Otherwise, hydrogen cannot truly be considered a 'green' technology.

2.2 Fuel cell and electrolyzer technologies

Fuel cells and electrolyzers are electrochemical devices that bridge the gap between chemical potential energy and electrical energy. In a fuel cell, this conversion is exothermic and spontaneous: a fuel (hydrogen) and an oxidant (oxygen) generate electrical power alongside water and heat. An electrolyzer runs this process in reverse, consuming electrical power to force a non-spontaneous cleavage of water molecules into hydrogen and oxygen. In both devices, the overall reaction is split into two half-reactions - a reductive reaction at the cathode and an oxidative reaction at the anode. These two half reactions are separated by an ion-conducting, electrically insulating membrane which forces the electrons to travel through an external circuit, generating a usable electrical current [16].

There are several types of fuel cells and electrolyzers, which are substantially defined by the electrolyte, charge carrier and operating temperature used. Table 2.1 summarizes several hydrogen fuel cell technologies. Table 2.2 summarizes several main hydrogen electrolyzer technologies.

Table 2.1: Comparison of fuel cell technologies [16, 27, 28].

Fuel Cell Type	PEMFC	AEMFC	PAFC	SOFC	AFC
Electrolyte	polymer	polymer	phosphoric acid	ceramic	alkaline solution
Charge carrier	H^+	OH^-	H^+	O^{2-} or H^+	OH^-
Fuel	H_2	H_2	H_2	H_2, hydrocarbons	H_2
Temperature °C	50-100	50-100	150-220	500–1000	60-90

Table 2.2: Comparison of water electrolyzer technologies [29, 30].

Electrolyzer Type	PEMWE	AEMWE	SOEC	AWE
Electrolyte	polymer	polymer	ceramic	alkaline solution
Charge carrier	H^+	OH^-	O^{2-} or H^+	OH^-
Reactant	H_2O	H_2O, KOH	H_2O	KOH, NaOH
Temperature °C	50-80	50-80	700-850	60-90

While there are several technologies for fuel cells and electrolyzers, because of their high power density and excellent transient response capabilities—which are critical for integration with variable renewable energy grids—this thesis will narrow its scope to focus strictly on proton exchange membrane (PEM) devices.

2.3 Electrochemistry of PEM devices

The fundamental operation of both PEM fuel cells and electrolyzers revolves around the same reversible electrochemical reaction: the synthesis and cleavage of water. The overall reaction can be expressed as:

$$H_2 + 1/2\, O_2 \rightleftharpoons H_2O \quad E^0 = 1.23\ V \tag{2.3}$$

Standard potentials are defined relative to the Reversible Hydrogen Electrode (RHE)

Under standard conditions (25°C and 1 atm), the reversible thermodynamic cell voltage (E^0) for this reaction is 1.23 V. To harness or drive this reaction, it must be physically separated by the proton exchange membrane into two distinct half-reactions occurring at the opposing electrodes.

The hydrogen half-reaction, which is the Hydrogen Oxidation Reaction (HOR) in a fuel cell or the Hydrogen Evolution Reaction (HER) in an electrolyzer, is kinetically very rapid.

The E^0 potential of the HOR (or HER) is 0 because this reaction is the same one taking place in the RHE it is measured against

$$H_2 \rightleftharpoons 2H^+ + 2e^- \quad E^0 = 0.00\ V \tag{2.4}$$

The oxygen half-reaction, which is the Oxygen Reduction Reaction (ORR) in a fuel cell or the Oxygen Evolution Reaction (OER) in an electrolyzer, is more complex and kinetically much slower. Because of this it can easily be rate limiting and requires more catalyst.

$$O_2 + 4H^+ + 4e^- \rightleftharpoons 2H_2O \quad E^0 = 1.23\ V \tag{2.5}$$

In a perfectly reversible system, a PEM fuel cell would output exactly 1.23 V, and a PEM electrolyzer would require exactly 1.23 V to split water. However, a loss-less device is unrealistic and in practice moving electrons and ions at a useful rate requires overcoming certain physical and chemical barriers. These barriers express themselves as overpotentials (η). The three primary sources of loss are listed below and illustrated in Figure 2.4.

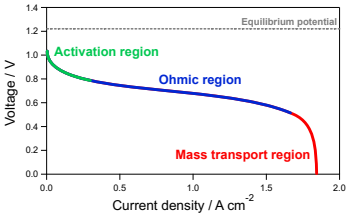

Figure 2.4: Example polarization curve for a PEM fuel cell with the regions dominated by activation losses, ohmic losses and mass transport losses marked.

- **I: Activation overpotential (η_{act}):** The kinetic energy required to overcome the activation energy barrier of the electrochemical reactions, which takes place at the catalyst site or interface.
- **II: Ohmic overpotential (η_{ohmic}):** The physical electrical resistance of the cell components such as electrodes or bipolar plates and the ionic resistance of the polymer membrane to proton transport.
- **III: Mass transport overpotential (η_{tx}):** The concentration losses that occur at high current densities when reactants cannot reach the active sites—or products cannot be evacuated—fast enough.

Because of these overpotentials, the practical operating voltage of a PEM device always deviates from the ideal thermodynamic

limit. In a fuel cell, these losses act as a penalty that *decreases* the available output voltage, meaning the cell produces less usable power than theoretically possible ($V_{\text{cell}} = E_{\text{rev}} - \sum \eta$). Conversely, in an electrolyzer, these losses act as additional resistance that must be overcome, *increasing* the voltage required to split water ($V_{\text{cell}} = E_{\text{rev}} + \sum \eta$).

In PEM devices, these reactions are always catalyzed. While HOR and HER are kinetically fast, the complex four-electron oxygen reactions (ORR and OER) are more sluggish. Minimizing their activation penalty dictates much of the material design of the cell, leading directly to the necessity of suitable electrocatalysts capable of delivering good performance. The majority of the catalyst is used for the ORR or OER electrodes [16, 29].

2.3.1 Catalysis

The hydrogen and oxygen reactions (equations 2.4 and 2.5) occur on heterogeneous electrocatalysts which provide an alternative reaction pathway with a significantly lower kinetic energy barrier (activation energy) than the uncatalyzed reaction. The general mechanism of a heterogeneous catalyst is:

1. **Adsorption:** reactants diffuse to the catalyst surface and bind to a free active catalyst site (denoted as $*$).
2. **Surface Reaction:** the adsorbates react while they are adsorbed, this can be a reaction in multiple steps as is the case in the OER mechanism.
3. **Desorption:** the final product leaves the catalyst site, returning to the bulk solution and leaving a free catalyst site again.

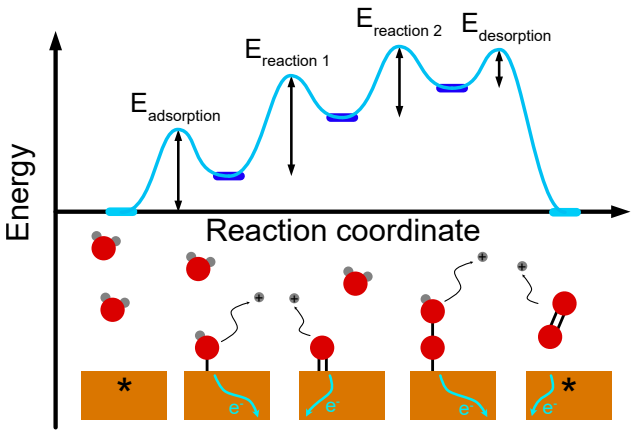

Figure 2.5: Free energy profile of the catalyzed OER reaction by the adsorbate evolution mechanism (AEM). The reaction steps (equations 2.8a-d) are referenced from [31].

By stabilizing the intermediate states on its surface, the catalyst lowers the peak energy required to drive the reaction, i.e. lowering the kinetic barrier of the reaction (Figure 2.5).

The hydrogen evolution reaction (HER) begins via a Volmer adsorption step (equation 2.6) in which a proton is reduced from the

electrolyte to form an adsorbed species on the catalyst surface.

The mechanisms described here are for acidic conditions.

$$\text{Volmer step:} \quad * + H^+ + e^- \rightleftharpoons H^* \tag{2.6}$$

The formation of H_2 then proceeds through one of two mechanisms: the Heyrovsky step, which takes an additional proton from solution, or the Tafel step which combines two adsorbed protons (equations 2.7a and b). The Heyrovsky mechanism occurs when the coverage of adsorbed hydrogen on the catalyst is low, the Tafel mechanism occurs at high coverages of adsorbed hydrogen [16].

$$\text{Heyrovsky step:} \quad {}^*H + H^+ + e^- \rightleftharpoons H_2 + * \tag{2.7a}$$
$$\text{Tafel step:} \quad 2{}^*H \rightleftharpoons H_2 + 2* \tag{2.7b}$$

Both the Volmer-Heyrovsky and Volmer-Tafel mechanisms are reversible, thus the hydrogen oxidation reaction (HOR) occurs through the same pathway in reverse.

The Oxygen Evolution Reaction (OER) typically occurs via the Adsorbate Evolution Mechanism (AEM).[1] This mechanism proceeds via four proton-electron transfer steps as shown in equations 2.8a-d and in figure 2.5 [29, 31]. The ORR reaction follows the reverse pathway.[2]

$$H_2O + * \rightleftharpoons {}^*OH + H^+ + e^- \tag{2.8a}$$
$${}^*OH \rightleftharpoons {}^*O + H^+ + e^- \tag{2.8b}$$
$${}^*O + H_2O \rightleftharpoons {}^*OOH + H^+ + e^- \tag{2.8c}$$
$${}^*OOH \rightleftharpoons O_2 + H^+ + e^- \tag{2.8d}$$

1: Another pathway is the Lattice Oxygen Evolution Mechanism (LOEM), in which oxygen from an Iridium oxide catalyst is consumed and then regenerated [32].

2: There is also a dissociative mechanism in which the oxygen molecule adsorbs and splits into two immediately similar to the Tafel step in the HER, but such a detailed discussion of ORR pathways and kinetics is beyond the scope of this thesis.

Every step of these mechanisms is defined by the bonding of intermediates to the catalyst surface (∗). In choosing a catalyst for a reaction, the binding energy of the catalyst and adsorbed species is paramount.[3] If the binding energy is too weak, the reactants will fail to adsorb to the surface, and the reaction will not initiate (e.g., gold or silver for hydrogen reactions). If the binding energy is too strong, the intermediates will form highly stable bonds and the products will not desorb, blocking ("poisoning") the active sites and halting the catalytic cycle (e.g., molybdenum or tungsten). This requirement for a catalyst which does not bond too strongly or too weakly is called the Sabatier principle, and is well illustrated with a volcano plot in which the activity of a catalyst is plotted against the binding energy of the catalyst for a given intermediate (Figure 2.6).

3: Alongside stability in the desired chemical environment.

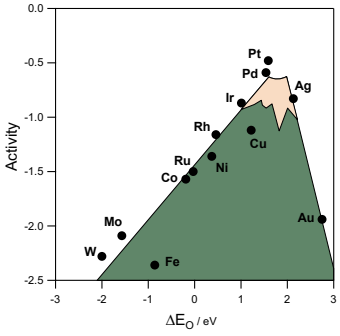

Figure 2.6: Sabatier volcano plot showing trends in the ORR activity as a function of the oxygen binding energy for various electrocatalysts. Data source: [33].

For the hydrogen reactions (HER/HOR), pure Platinum shows the highest activity and is placed nearest the peak of the volcano, which is why Platinum is used as the electrocatalyst of choice for the HER and HOR reactions. For the ORR reaction, Platinum is also preferred for similar reasons (Figure 2.6). However, for the

OER a different catalyst, Iridium oxide, is used despite the fact that the OER mechanism is reversible, which usually means the same catalyst is optimal. This is because the ORR/OER mechanism is a multi step process and different steps are rate limiting in the forward and backwards directions.

In the ORR reaction, the rate (and overpotential) is determined by the adsorption of oxygen and the cleavage of the O=O bond, thus the catalyst is determined by the binding energy of $^*O$ on the catalyst surface [33]. For the OER reaction, the rate limiting step is the formation of the $^*OOH$ intermediate from adsorbed $^*O$ (equation 2.8c) and the catalyst is determined by the binding energies of the $^*OH$ and $^*OOH$ intermediates [34]. This is why a different catalyst, Iridium oxide, is needed. Because Iridium is an extremely scarce element, there is a major drive to reduce the loading required in the OER electrode.

Ruthenium oxides actually show better OER activity than Iridium oxides, but are unfortunately not chemically stable under OER conditions.

2.4 PEM fuel cell and electrolyzer components

Proton exchange membrane (PEM) fuel cells and electrolyzers are among the most well-researched electrochemical energy conversion devices. Operating continuously below 100 °C, they are classified as low-temperature technologies (Tables 2.1 and 2.2). The overall operating schematics of a fuel cell and electrolyzer were shown previously in figure 1.3. The 'heart' of either device is the membrane-electrode assembly (MEA), in which the reactions take place and which must also facilitate transport of the reactants to the catalyst sites, and of products from the catalyst sites.

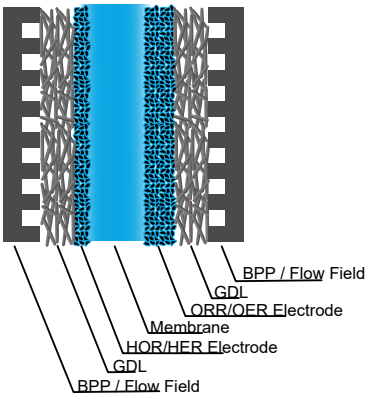

Figure 2.7: General membrane-electrode assembly (MEA) schematic with bipolar plates.

The MEA represents the primary materials science challenge for PEM devices. In each case the MEA consists of a proton exchange membrane in the center, which is made of an ionomer like Nafion; electrodes to either side, which contain ionomer, catalyst, and a support structure. Bipolar plates then act as current collectors separating different cells in the fuel cell or electrolyzer and are also shaped to act as a flow field. The MEA layers are schematically illustrated in figure 2.7 [16].

The electrode support structure is typically carbon, except in the case of the OER electrode in an electrolyzer as carbon will corrode here. At the OER electrode, Titanium is typically used instead and is often coated in a layer of Platinum to prevent the formation of a non-conductive titanium oxide layer. The same material choices apply for the gas diffusion layer or the porous transport layer, and to the bipolar plate [29].

2.4.1 Proton exchange membranes

PEM fuel cells and electrolyzers use a solid polymer electrolyte membrane in order to function, which must be electrically insulating while being conductive to protons and preventing the crossover of reactant gases, especially hydrogen. This is accomplished by using an ionomer, a hydrophobic polymer chain which features side chains ending in sulfonic acid groups. The most common ionomer is Nafion (Figure 2.8a). When hydrated, the sulfonic acid groups arrange themselves internally to form channels because they are the only hydrophilic part of the ionomer (Figure 2.8b).

These channels create an acidic environment that can conduct protons when hydrated[4] [35].

Proton conduction through an ionomer membrane can occur through two mechanisms. In the vehicular mechanism, protons bind to water molecules to form H_3O^+ ions and diffuse through the fluid. In the Grotthuss mechanism, protons exchange place between water molecules and the fixed $-SO_3^-$ sites. This means that as a proton is withdrawn from the membrane, a cascade occurs along the hydrogen bond network, allowing a new proton to be accepted from the opposite side [36].

4: When insufficiently hydrated, the channels shrink, resulting in individual sections that are not connected and are thus unable to conduct protons across the membrane.

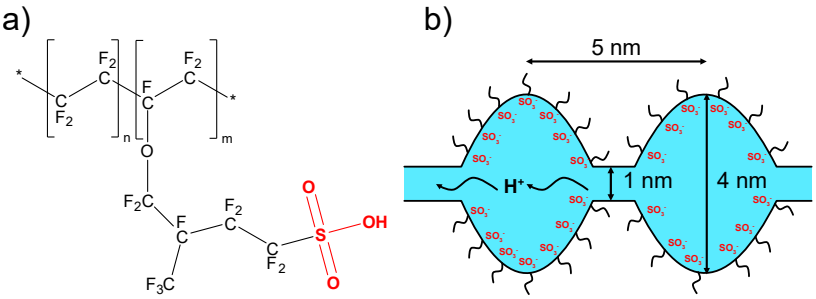

Figure 2.8: a) Chemical structure of Nafion, the most common PFSA ionomer. b) Model of the proton-conducting cluster networks in a hydrated proton exchange membrane. The $-SO_3^-$ active groups are marked in red. Data source: [36, 37].

2.4.2 HER/HOR electrodes

The Hydrogen Oxidation Reaction (HOR) and the Hydrogen Evolution Reaction (HER) follow the same relatively simple, reversible mechanism and use the same catalyst, platinum (see chapter 2.3.1). The construction of the HOR and HER electrodes is effectively identical, consisting of a 5-15 μm layer of a porous carbon with a low loading of platinum nanoparticles[5] held together by an ionomer which acts as both a physical binder and proton conductor. The porous, conductive support and the ionomer create a three-phase boundary around the platinum nanoparticles which is required for the reaction to take place.

5: The loading of platinum on the HOR and HER electrodes is relatively low due to the fast kinetics of these reactions, typically around 0.1 mg_{Pt}/cm^2, as a high turnover rate means a lower amount of catalyst is required [38]. Because of the low loading, the carbon support for the HER and HOR electrodes does not need to be a high surface area carbon.

The HOR or HER electrode is manufactured by coating a catalyst ink onto the membrane. The catalyst ink is a mixture of the platinum nanoparticles supported on carbon together with an ionomer, dispersed in a solvent which is typically a mixture of water and isopropyl alcohol. After applying the ink to the membrane via, for example, ultrasonic spray coating, heat and pressure are applied to bond the ionomer in the ink to the particles and to the membrane [16, 29]. Figure 2.9 illustrates the composition of a typical fuel cell electrode made in this way.

2.4.3 ORR/OER electrodes

The construction of the fuel cell ORR electrode is similar to the HOR/HER electrodes, consisting of a porous carbon support,[6] an ionomer binder, and platinum nanoparticles. However, the

6: The support for the ORR is typically a high surface area carbon. The high surface area is needed to support the higher catalyst loading.

ORR electrode requires a much higher platinum loading (typically around 0.4 mg_{Pt}/cm^2) [38]. The resulting catalyst layer is thicker than its hydrogen counterpart to accommodate the required catalyst volume while maintaining adequate porosity for reactant gas and product water transport [28].

In an electrolyzer, the highly oxidative conditions required to drive the OER (> 1.5 V vs. RHE) are capable of corroding carbon into CO_2 gas. This prevents the use of carbon supports, and so the OER electrode relies on titanium instead for structural support and electron conduction. There are two main types of OER electrode:

1. **Catalyst Coated Membrane (CCM):** Similar to the ORR electrode, an ink is formulated using an ionomer and the catalyst. Because carbon cannot be used, the ink consists of either unsupported IrO_2 nanoparticles or iridium supported on corrosion-resistant titanium. The ink is coated directly onto the membrane, for example by ultrasonic spray coating, and a separate titanium Porous Transport Layer (PTL) is pressed against it during cell assembly. This approach is more common, but will result in interfacial resistances between the titanium PTL and the iridium catalyst as the titanium forms a passivating oxide layer [29].
2. **Porous Transport Electrode (PTE):** The catalyst is deposited directly onto the titanium PTL (which typically consists of sintered titanium grains or fibers). To prevent the titanium from passivating, a protective interlayer of platinum is deposited on the titanium upon which the active iridium catalyst is then applied (Figure 2.10). The application of the platinum and iridium layers typically occurs by atomic layer deposition (ALD), chemical vapor deposition (CVD), sputtering, or electrodeposition. PTEs with and without ionomer have both shown good performance [39].

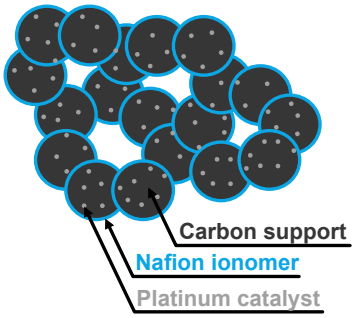

Figure 2.9: Illustration of a typical fuel cell electrode composed of platinum nanoparticles on a carbon support bound together with an ionomer.

Figure 2.10: Layers in a PTE.

2.4.4 Gas diffusion and porous transport layers

The gas diffusion layer (GDL) or porous transport layer (PTL) is responsible for the bulk transport of reactant gases to, and product gases from, the electrode. It must also conduct electrons between the bipolar plate and the electrode [40]. The primary distinction between a GDL and a PTL arises from their liquid water management requirements. In an electrolyzer, water is actively consumed at the OER electrode. Thus, the transport layer at the OER electrode must transport liquid water to the reaction site as well as facilitate gas transport away from it. This is the porous transport layer (PTL), which is typically made of titanium grains or fibers [29].

At the HER electrode, and at both electrodes in a fuel cell, water must instead be removed to prevent flooding. Because of this, the GDL applied to these electrodes includes a hydrophobic element,

There are three typical carbon fiber architectures used in GDLs: non-woven carbon fiber felts (tangled fibers), woven carbon cloths, or rigid carbon papers (straight fibers held together by a carbonized resin).

typically polytetrafluoroethylene (PTFE), which is absent in a PTL. The GDL macrostructure is typically made of carbon fibers and has a high porosity to facilitate gas diffusion [41].

Typically, the carbon fibers are of significantly greater size than the porous carbon used in the electrode, and so a microporous layer (MPL) is applied to the GDL on the side facing the electrode. The MPL exists to bridge the difference in length scales between the GDL and the electrode, and consists of a similar porous carbon to the one used in the electrode, held together with PTFE acting as a hydrophobic agent and binder [40].

2.4.5 Bipolar plates (BPP)

The bipolar plates (BPPs) are the electrical bridge between adjacent cells, collecting the current between the anode of one cell and the cathode of the next. They need to have a high through-plane conductivity (though not necessarily in-plane conductivity), be chemically resistant to the electrochemical environment they are in, and also act as a flow field directing gas flow to and from the GDL or PTL [28]. [7]

7: The current collector in stack terminology is a separate component at the ends of the stack rather than between individual cells. It connects the stack to the external power system and is usually made out of copper as it is not in contact with a cell's electrochemical environment and must provide good conduction in-plane as well as through-plane.

For PEM fuel cells, highly graphitic carbon or carbon-polymer composites are traditionally used for the BPP, though coated metallic plates are increasingly adopted to further reduce stack volume and cost [42, 43]. In PEM electrolyzers, the extreme anodic potentials require titanium instead, which is coated with a protective layer of platinum or gold [30, 44].[8] In a commercial stack, the BPP is kept as thin as possible to reduce material costs and stack volume while remaining thick enough to support the mechanical compression of the stack and contain flow channels sufficient for the gas flow to and from the GDL.

8: This coating is required to prevent passivation of the titanium through the formation of a resistive TiO_2 layer [29].

The BPP represents the largest difference between commercial stacks and lab-scale single-cell testing. In laboratory environments, the BPPs are deliberately massive and over-dimensioned so that mechanical compression is uniform and the fluid transport through the flow field is never the limiting factor in the cell's performance [28].

2.5 Operations and economics of fuel cells and electrolyzers

Besides the materials and roles of the components in PEM devices, it is also important to consider the relative cost of the components as well as what operating conditions the device and its components are expected to see.

In a representative 1 MW PEM water electrolyzer (PEMWE) installation, the bipolar plates (BPPs) and the porous transport layers

(PTLs) are the largest cost drivers, followed by the electrodes and catalysts. By contrast, in a typical 80 kW PEM fuel cell (PEMFC) system for automotive use the electrode and catalyst are the greatest material cost drivers, followed by the bipolar plates (Figure 2.11). As discussed in section 2.4.5, the BPP for an electrolyzer requires platinum or gold coatings that are not required for a fuel cell and which significantly impact their cost [45, 46].

Operationally, PEMFCs are defined by highly variable, dynamic loading requirements. Whether deployed in automotive roles or responding to grid balancing signals, a fuel cell stack must rapidly cycle between low-current idling and peak power density, a process that induces continuous mechanical and chemical fluctuations across the membrane-electrode assembly (MEA). By contrast, PEMWE systems generally operate under relatively constant, high baseloads to maximize hydrogen generation.[9] Electrolyzers operate with a high degree of electrochemical compression within the cell because they are required to produce hydrogen at high purity and at high pressure. This means that the components of an electrolyzer, particularly the membrane, are subject to very high pressure differentials.[10][45, 46]

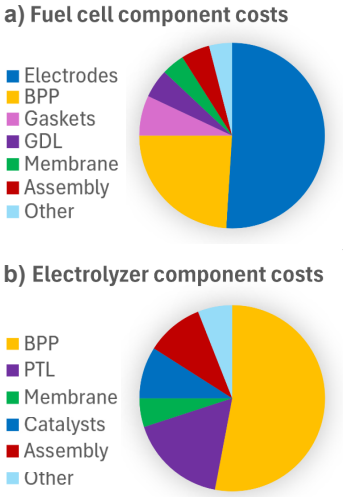

Figure 2.11: a): Component cost breakdown of the stack cost distribution within as 80 kW automotive PEM fuel cell system, data source: [46]. b): Component cost breakdown of a representative 1 MW PEM WE installation, data source: [45]. Note that the methodologies of the two sources are not the same, so only a qualitative comparison is possible.

2.6 Durability

A primary bottleneck to the commercialization of PEM devices is their long-term durability. Systems are not commercially viable if they require premature replacement due to degradation, and the components in PEM devices are subject to very harsh conditions. The catalysts are subject to several distinct degradation pathways: Ostwald ripening, in which catalyst atoms dissolve and migrate from smaller particles to larger ones, thereby decreasing the total available active surface area; particle coalescence, where adjacent nanoparticles migrate and fuse together into larger agglomerates with a reduced surface; dissolution, where platinum ions dissolve directly into the ionomer phase; and physical detachment from their support structures, a process heavily hastened if the carbon support structures themselves undergo electrochemical corrosion. The polymer membrane also experiences chemical degradation, where radical attack causes the loss of functional sulfonic acid groups and lowers ionic conductivity, as well as mechanical degradation due to hygrothermal expansion and contraction which causes the membrane to thin or form pinholes. The bipolar plates and porous transport layers are susceptible to severe passivation due to the formation of an oxide surface layer that increases interfacial contact resistance, as well as corrosion [28, 29, 47].

PEM devices are nonetheless required to operate for extended periods of time. By 2050, the International Renewable Energy Agency has set the target operational lifetime for a PEM electrolyzer at 100,000 to 120,000 hours [45]. For fuel cell applications,

9: Such constant operation is, of course, not compatible with demand-side stabilization of an electricity grid. Future electrolyzers might need to vary their load to a greater extent than current ones.

10: IRENA has set operating targets for 2050 at 4-6 A/cm^{-2} at < 1.7 V, producing hydrogen at 70 bar pressure and $> 99.9\%$ purity [45].

the European Union's 2030 target aims for an operational lifespan of 30,000 hours [48]. As testing a device for even 1,000 hours requires over a month of continuous, uninterrupted laboratory operation, validation of a 30,000- or 100,000-hour lifespan is unrealistic even on nearly complete systems. Accelerated Stress Tests (ASTs) subject the device to extreme electrochemical cycling, elevated temperatures, or aggressive humidity swings to rapidly induce specific degradation mechanisms in a fraction of the time. These can help to mitigate such long testing periods, but are not always representative of actual operating conditions. Durability and durability testing are therefore one of the most challenging areas of development for PEM devices [47].

Methods 3

Following the previous section on fuel cell and electrolyzer fundamentals, this section will introduce the sample preparation and characterization methods used in Paper I and Paper II.

3.1 Confocal Raman spectroscopy 15
3.2 Electron microscopy . 15
3.3 Identical location methods 17
3.4 Electrochemical characterization 18
3.5 Gas physisorption surface area analysis . 20
3.6 Sample preparation . 21
3.6.1 Gas diffusion layers . . 21
3.6.2 Carbon nanofiber porous transport electrodes 22

3.1 Confocal Raman spectroscopy

When light interacts with matter, the vast majority of photons undergo elastic Rayleigh scattering, in which the scattered light retains the same energy and wavelength as the incident light. A small portion of the photons, roughly 1 in 10^7, undergoes inelastic Raman scattering. The Raman scattered photons possess a different energy and wavelength than the incident photons because the incident photon interacts with the electrons in the molecule, inducing a temporary dipole moment if the affected electron is part of a polarizable chemical bond. The interaction can be described as an excitation followed by a deexcitation to a shifted energy level (Figure 3.1). The resulting shift in the scattered photon's energy is dependent on the polarizable bond of the electrons in question, and therefore is specific to that bond [49].

To exploit this, we need a monochromatic light source such as a laser, which has only a single wavelength.[1] The scattered light is collected, the incident light wavelength is blocked and the remaining Raman scattered light, which has a different wavelength, is analyzed. By putting the laser into a confocal optical microscope, a single, localized focal point can be viewed, and by analyzing many individual points a chemical map can be generated.

In this work, Raman spectra and maps were acquired using a Renishaw inVia Reflex confocal Raman microscope equipped with a motorized XYZ stage. Measurements were primarily conducted using a 785 nm excitation laser with a maximum power of 300 mW, paired with a 1200 l/mm diffraction grating, providing a spectral resolution of better than 2 cm^{-1} at a spatial resolution better than 2 μm. 532 nm and 633 nm lasers are also available on this system.

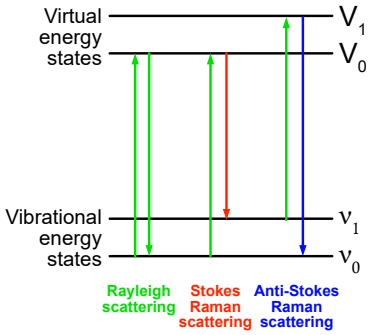

Figure 3.1: Energy level diagram illustrating Rayleigh scattering alongside Stokes and anti-Stokes Raman scattering. Note that anti-Stokes scattering requires a significant population of electrons to be in the v_1 vibrational state, which occurs at high temperatures.

3.2 Electron microscopy

To understand how materials function it is imperative to understand their micro- and nanostructure, which is difficult because the required resolution is smaller than the wavelength of light for optical microscopes. Therefore, we use electrons instead of light, as when sufficiently accelerated electrons have a de Broglie

1: The intensity of Raman scattering is inversely proportional to the fourth power of the excitation wavelength ($\propto 1/\lambda^4$). While shorter wavelengths scatter much more efficiently, they also carry a significantly higher risk of inducing competing fluorescence, which can easily drown out the inherently weak Raman signal.

wavelength in the sub-nanometer range.[2] An electron microscope is therefore able to provide substantially better resolution than an optical system, with transmission electron microscopes (TEM) in particular being notable for providing atomic scale resolution.

Electron microscopes operate by producing electrons from a Schottky field emission gun or other source, accelerating them through an electric field, and focusing the resulting electron beam through a series of magnetic lenses. In a scanning electron microscope (SEM), the electron beam is scanned across the surface of a sample. Transmission electron microscopy (TEM) and scanning transmission electron microscopy (STEM) use highly accelerated electron beams that pass through the sample, which must be extremely thin.[3] While TEM uses a wide electron beam to image a whole field of view simultaneously, STEM focuses the transmitted electrons into a narrow probe that is scanned across the sample. This rastering capability in STEM enables spatially resolved techniques such as high-angle annular dark-field (HAADF) imaging and chemical mapping by EDX. Figure 3.2 illustrates the beam paths and detectors for an SEM [50, 51].

2: The de Broglie wavelength $\lambda = h/p$, with the planck constant h and electron momentum p, is about 0.017 nm for an electron accelerated at 5 kV.

3: A TEM sample will usually be 100 nm thick or less.

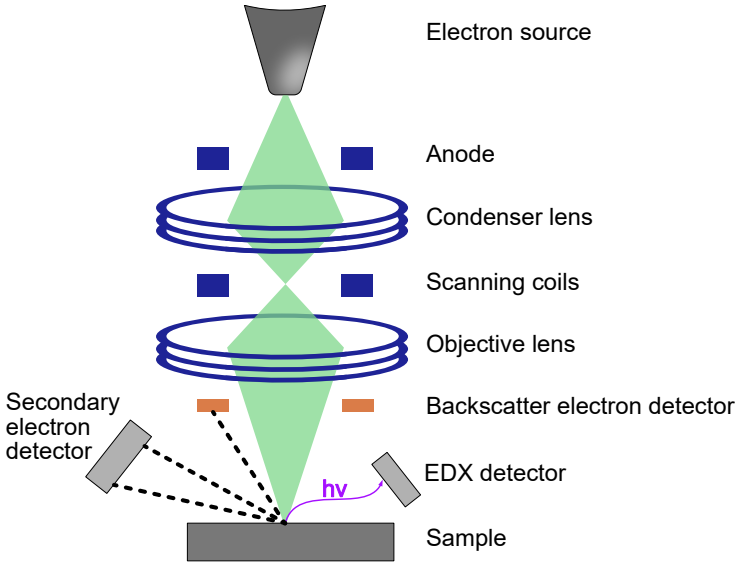

Figure 3.2: Schematic illustration of a scanning electron microscope.

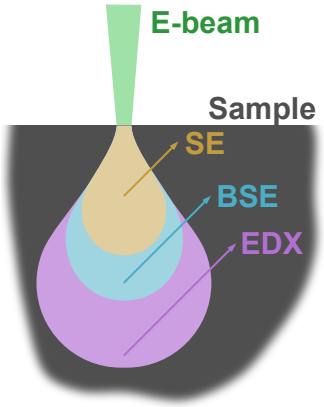

Figure 3.3: Interaction volumes in a sample for secondary electrons (SE), backscattered electrons (BSE), and characteristic X-rays (EDX) [52].

The electron-matter interactions in an electron microscope allow for several analytical techniques. Secondary electrons (SEs) are generated via inelastic scattering of the incident electrons, which eject loosely bound outer-shell electrons from atoms within the sample, which in turn can eject outer-shell electrons they encounter. These ejected electrons are called secondary electrons, and can near-surface secondary electrons can escape the sample and reach the detector. Because of their low kinetic energy, SEs escape only from a shallow depth, resulting in a small interaction volume suitable for topographic imaging of a sample (Figure 3.3). Secondary electrons are the primary imaging mode for SEMs [50].

Backscattered electrons (BSEs) are a product of elastic scattering, high-angle deflections that occur when an incident electron collides directly with an atomic nucleus in the sample. The probability

of backscattering is much greater for elements with a high atomic number (Z), so heavier elements backscatter electrons more efficiently and appear distinctly bright. The interaction volume for BSE is larger than that for SEs. In STEM, heavier elements can be similarly enhanced with high-angle annular dark field imaging HAADF-STEM imaging, which uses an annular detector to exclusively capture electrons that have collided with atomic nuclei and scattered. Enhancing the contrast of heavier elements is useful when, for example, imaging noble metal catalysts on a carbon support [50, 51].

Energy-dispersive X-ray (EDX) spectroscopy operates as a direct product of the inner-shell electron displacements initiated during SE generation. When a core-shell electron is ejected, it leaves behind an unstable vacancy or core hole. An electron from a higher-energy outer shell relaxes to fill this vacancy, releasing its excess energy as an X-ray photon. The energy of this emitted X-ray is uniquely determined by the electronic transitions of the atom involved which enables elemental identification (see figure 3.4). For SEM and STEM, scanning across a sample while collecting EDX signals enables elemental mapping, though notably the interaction volume for EDX is significantly larger than for SE or BSE imaging. [50, 51]

EDX requires the incident electrons to have sufficient energy to dislodge electrons in the sample atoms, typically requiring an accelerating voltage 2-3 times higher than the K_α energy of an element for a good signal. The high accelerating voltage also inflates the interaction volume of EDX, which is ca. 1 μm in carbon for a 10 kV acceleration voltage [53].

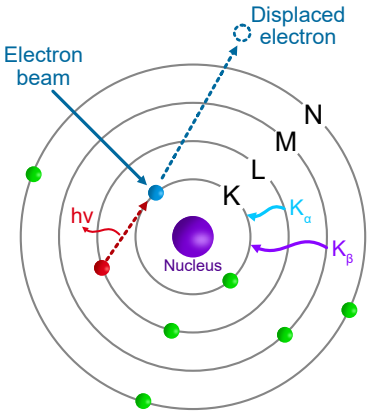

Figure 3.4: Electronic shell transition diagram for EDX, showing the emission of characteristic K_α and K_β X-ray photons.

Focused Ion Beams (FIB) are integrated as a dual-beam system within an SEM chamber. In a FIB, a focused beam of heavy ions (in our case, Ga^+) is focused on the sample to precisely sputter away material on a micrometer scale. This is useful for sample preparation and for making cross-sections to analyze the subsurface microstructure of samples. Milling shallow angles relative to the interface plane has been particularly useful in this work, as this artificially stretches out the vertical height profile across a broader lateral distance, magnifying thin interfacial layers and boundaries for analysis with techniques like Raman that have a lower resolution [54].

All electron microscopy instrumentation utilized in this work was accessed through the Chalmers Materials Analysis Laboratory (CMAL). The SEMs used were a Zeiss Ultra 55 and a JEOL 7800F Prime SEM, which is equipped with an Oxford Instruments X-MaxN 50 EDX detector. FIB work was carried out using a FEI Versa3D dual-beam FIB-SEM. TEM work was done on a FEI Titan 80-300 TEM/STEM. Typical accelerating voltages were 5 kV for primary SEM imaging, 25 kV for SEM-EDX operation, and 300 kV for TEM and STEM operation.

3.3 Identical location methods

Identical location (IL) methods allow the exact same microscopic region of interest to be repeatedly analyzed before and after as-

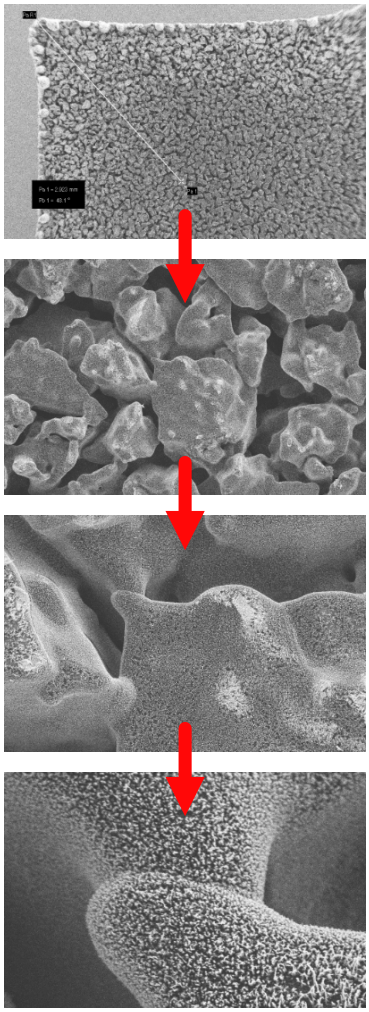

Figure 3.5: Sequential images demonstrating the process of zooming in on an identically located spot on an SEM sample.

The development of the identical location methods described here was my own, though it was significantly inspired by the work of Linnéa Strandberg [55].

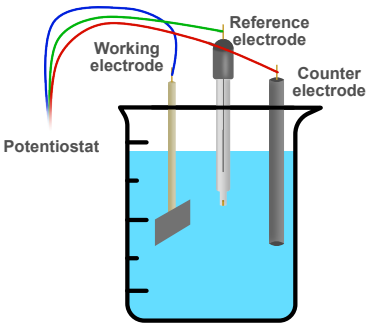

Figure 3.6: Schematic of a standard ex-situ three-electrode electrochemical cell.

sembly or disassembly of a MEA (or another process) and across different instruments. The procedure relies on establishing a reliable macroscopic reference point, such as a marked corner of the sample, to define a consistent coordinate system and orientation. From this origin, the relative coordinates of a region of interest are mapped,with a sequential series of images captured at increasing magnifications to help in relocating the region (Figure 3.5). Navigating back to the same site is made significantly easier by distinctive local features, such as specific fiber orientations and binder clusters in a gas diffusion layer (GDL) or uniquely shaped grains in a porous transport electrode (PTE). This is especially relevant when looking at a sample with very different instruments such as SEM and a confocal Raman microscope.

In this work, IL techniques were also used to correlate between a PTE and its corresponding physical imprint on the polymer membrane in an electrolyzer assembly. Because the membrane and the PTE face each other during assembly, the coordinate system and the resulting imprints on the membrane are mirrored relative to the original PTE surface. Furthermore, the membrane imprint only captures the uppermost protruding features of the PTE grains, meaning parts of the PTE structure are not represented in the membrane topography, confusing the image. Due to these limitations, locating a specific feature is generally easier when tracing from the membrane imprint back to the PTE. However, this approach is incompatible with pre-assembly IL baseline imaging of the PTE. This can be overcome by selecting and mapping elevated PTE grains with distinct geometries or features prior to cell assembly. Once the cell was disassembled, the mirrored coordinates were calculated from the reference corner, and these distinctive "anchor" grains were located on the membrane. Adjacent features could be readily mapped once one anchor point had been identified.

3.4 Electrochemical characterization

Electrochemical characterization is necessary to evaluate fuel cell and electrolyzer performance. In this work, ex-situ three-electrode cells and in-situ single-cell test benches were used for this purpose.

The ex-situ three-electrode cell is a model system used to evaluate a single catalyst layer, and is set up as illustrated in Figure 3.6. This setup consists of a working electrode (the sample), a counter electrode (such as a platinum mesh or wire), and a reference electrode (such as a Silver/Silver Chloride (Ag/AgCl) electrode) which possesses a stable, reversible thermodynamic potential and passes negligible current, providing a constant baseline against which the working electrode potential can be precisely measured. The three-electrode system is fully submerged in a liquid electrolyte, such as dilute H_2SO_4. While this configuration provides excellent baseline

catalyst data, it is fundamentally limited by low measurable currents and an inability to reflect real-world operating environments. Specifically, it cannot be used to investigate interfacial contact resistances, gas-phase mass transport, or membrane hydration states. In-situ testing utilizes a single-cell test bench with all functional layers of the membrane electrode assembly (MEA).[4] It operates under system realistic conditions, allowing for precise control over reactant gas flows, operating temperatures, and relative humidity, although the flow fields are usually over-dimensioned compared to final stack designs, as discussed in chapter 2.4.5 [16, 56].

4: In-situ testing uses a smaller MEA than commercial systems, but overall the setup and testing is kept as close to a real-world device as possible.

Between three-electrode cells and in-situ testing, a variety of electrochemical methods can be used to analyze a sample. The polarization curve is the most fundamental diagnostic tool for in-situ MEA evaluation. By sweeping the applied current density and measuring the resulting cell voltage (or vice versa), the overall cell performance can be mapped. The resulting curve is characterized by three distinct loss regions: kinetic activation losses at low current densities, purely ohmic resistance in the linear mid-region, and mass transport limitations at high current densities. Typical polarization curves for fuel cells and electrolyzers are shown in figure 3.7 [16].

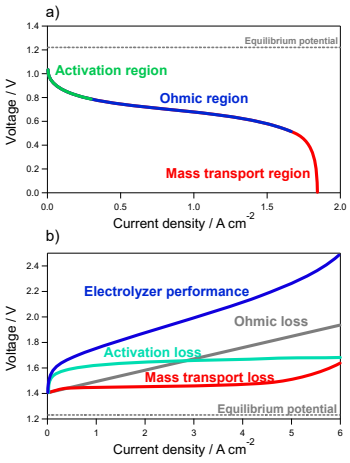

Figure 3.7: Typical a) fuel cell and b) electrolyzer polarization curves illustrating the activation, ohmic, and mass transport loss regions.

The mass transport resistance within a fuel cell oxygen-side GDL can be assessed by the limiting current method developed by Baker et al. [57]. By starving the oxygen electrode and increasing the current, the cell becomes entirely limited by mass-transport. The limiting current, i_{lim}, is the current in the resulting polarization curve where the voltage drops vertically. The total oxygen transport resistance, $R_{\text{tot}}^{\text{O}_2,\,\text{dry}}$, is then calculated using the following relation:

$$R_{\text{tot}}^{\text{O}_2,\,\text{dry}} = \frac{4 \cdot \mathcal{F} \cdot \chi^{\text{O}_2,\,\text{dry}}}{i_{\text{lim}}} \cdot \frac{p - p_w}{\mathcal{R} \cdot T} \tag{3.1}$$

where $\mathcal{F}$ is Faraday's constant, $\chi^{\text{O}_2,\,\text{dry}}$ is the dry inlet oxygen mole fraction, p is the absolute gas pressure, p_w is the partial pressure of water vapor (calculated via the relative humidity and the Antoine equation), $\mathcal{R}$ is the ideal gas constant, and T is the absolute temperature. By assuming a linear dependence of R_{tot} on pressure, the total resistance can be deconvoluted into a pressure-dependent term representing intermolecular diffusion resistance (R_{P}), and a pressure-independent term representing Knudsen diffusion in the catalyst layer and interfacial resistance (R_{NP}). This deconvolution is represented in figure 3.8. This experiment requires an in-situ cell.

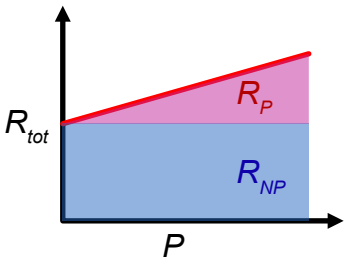

Figure 3.8: Drawing of the total oxygen transport resistance as a function of absolute pressure, illustrating the deconvolution of R_{P} and R_{NP}.

Constant current hold (chronopotentiometry) is a straightforward stability test where the in-situ cell is forced to hold a specific steady-state current, and the voltage is continuously monitored over time. It is a good representation of steady-state operation, and its primary drawback is the extensive duration required to observe

meaningful degradation, often taking hundreds or thousands of hours [29].

Cyclic voltammetry (CV) is a transient technique applicable to both ex-situ and in-situ setups. The applied potential is swept linearly back and forth between two voltage limits while the resulting current is measured. This provides electrochemical information about the catalyst, including the active surface area, oxidation/reduction peaks, and reaction reversibility. Repeated, rapid CV cycling is also a standard method for conducting Accelerated Stress Tests (ASTs) [56].

Tafel slope analysis is used in a three-electrode cell to isolate the kinetics of a single electrode. The relationship between the applied overpotential (η), which is the difference between the measured potential and the thermodynamic equilibrium potential, and the resulting current density (i) is described by the Tafel equation:

$$\eta = A \cdot \log_{10}\left(\frac{i}{i_0}\right) \tag{3.2}$$

where A is the Tafel slope and i_0 is the exchange current density, which is the current density at zero overpotential. By plotting η against $\log_{10}(i)$, the Tafel slope can be extracted from the linear regime of the plot, providing information about the catalyst's kinetic efficiency. This is shown in Figure 3.9 [56].

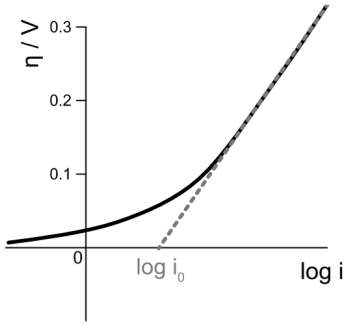

Figure 3.9: A standard Tafel plot (η vs. $\log i$) used to extract the Tafel slope and exchange current density.

Electrochemical Impedance Spectroscopy (EIS) is a technique where a small alternating current (AC) sine wave perturbation is superimposed over a baseline voltage or current, and the amplitude and phase shift of the system's response are measured. By sweeping this perturbation across a wide spectrum of frequencies, the complex impedance of the cell is calculated. The data is commonly visualized on a Nyquist plot (see Figure 3.10), mapping the real versus imaginary impedance. Different frequency domains correspond to distinct physical phenomena; for instance, high-frequency intercepts indicate ohmic resistance, semi-circles denote charge-transfer resistance, and low-frequency linear tails represent mass-transport diffusion limitations. EIS is a very complex tool that can offer a lot of information, but is usually very difficult to analyze [56].

The real axis of a Nyquist plot represents resistance, the imaginary part a combination of capacitance and inductance.

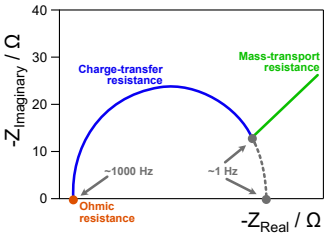

Figure 3.10: A representative Nyquist plot for an EIS experiment, showing typical ohmic, charge-transfer and mass-transport impedance features.

The instrumentation used for electrochemical analysis is detailed in the manuscripts as necessary.

3.5 Gas physisorption surface area analysis

Fuel cell and electrolyzer electrodes are porous structures, and it is often important to understand their specific surface area. We can obtain the total surface area of a sample if we know how much of an analyte gas (adsorbate) is adsorbed by the surface. Certain

analyte gases, such as Nitrogen and Krypton, will at cryogenic temperatures physisorb onto an available surface.[5] When dosing an adsorbate into an evacuated chamber with a sample, the pressure drops from two effects: the adsorbate gas fills the new volume of the container, and the it adsorbs onto the surface of the sample. To deconvolute these two effects, an initial dosing is performed with Helium, which does not adsorb, to determine the empty volume of the sample chamber. Dosing measurements are then performed at different pressures with the analyte gas to determine the amount of gas adsorbed by the sample surface as a function of pressure at constant cryogenic temperature. The resulting BET isotherm is shown in Figure 3.11.

5: Nitrogen is most typically used as an adsorbate. In my experiments, the specific surface area was relatively low, therefore Krypton was used instead. Krypton is more suitable for samples with low specific surface areas because it has a significantly lower vapor pressure than Nitrogen, and therefore the relative pressure drop following adsorption is higher.

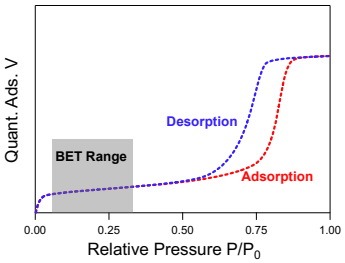

Figure 3.11: Diagram illustrating adsorption and desorption isotherms for a porous material, with the valid range for applying the BET theory shaded.

The specific surface area can be obtained from the Brunauer-Emmett-Teller (BET) theory, a mathematical model that accounts for both initial monolayer coverage and the subsequent formation of multiple adsorbate layers on the material's surface [58]. The BET equation is given in equation 3.3, where P and P_0 are the equilibrium and saturation pressure of the adsorbate, V is the total adsorbed gas quantity, V_m is the monolayer adsorbed gas quantity and c is the BET constant. V_m can be obtained by applying equation 3.3 to an adsorption isotherm, following which the sample surface area can be obtained by equation 3.4, where N_A is the Avogadro number and σ is the surface area of the adsorbate.

$$\frac{P}{V\,(P_0 - P)} = \left(\frac{c-1}{V_m c}\right)\left(\frac{P}{P_0}\right) + \frac{1}{V_m c} \tag{3.3}$$

$$S_{\text{total}} = \frac{V_m N_A \sigma}{V} \tag{3.4}$$

The saturation vapor pressure of an adsorbate is very sensitive to thermal fluctuations, and so cryogenic baths and isothermal jackets are required to obtain reliable BET surface area measurements. Even then, fluctuations in ambient pressure can change the bath temperature sufficiently to skew results if not accounted for.

The instrumentation used for surface area analysis was a Micro-Active ASAP 2020 Plus system.

3.6 Sample preparation

This section provides a brief overview of the sample preparation methods used in this thesis. More detailed descriptions of the sample preparation methods can be found in the relevant manuscripts and supplementals.

3.6.1 Gas diffusion layers

The gas diffusion layers (GDLs) used in paper I were prepared by treating them with polytetrafluoroethylene (PTFE) in order to make them hydrophobic. This was done by immersing the bare GDL substrates into diluted PTFE dispersions and varying the dipping time and concentration to reach the target PTFE loadings. The GDL samples were dried on absorbent paper and then heat

treated in a ventilated oven above the glass transition of PTFE, and held at elevated temperatures for 20 minutes. This let the PTFE soften and bond to the carbon fibers in its preferred configuration, and also ensured the complete removal of the organic emulsifiers in the dispersion.[6] Upon cooling, the PTFE loading of each sample was obtained gravimetrically.

6: The thermal treatment temperature was chosen at 380 °C, well above the glass transition temperature of PTFE around 130 °C [59] but below the rapid decomposition temperature at 400 °C [60].

3.6.2 Carbon nanofiber porous transport electrodes

The carbon nanofiber (CNF) porous transport electrodes in Paper II were provided by Smoltek Hydrogen AB, who are a project partner within the Swedish electricity storage and balancing center (SESBC). The nanofibers were grown onto a sintered titanium substrate. After cleaning, the substrates were sputtered with thin layers of titanium and titanium nitride to ensure low electrical resistance and provide a stable adhesion surface. A palladium nucleation layer was subsequently deposited via physical vapor deposition (PVD), the carbon nanofibers were then grown via plasma-enhanced chemical vapor deposition (PECVD), after which a protective layer of platinum was applied over the grown fibers using atomic layer deposition (ALD) [61].

The active iridium catalyst was then applied to the CNF by electrochemical deposition with the sample in a half-cell setup. The sample was transferred to a hot plate and a diluted Nafion ionomer solution was drop-cast onto it. Full membrane electrode assemblies (MEAs) were fabricated by hot-pressing the prepared anode, a polymer membrane, and a cathode. After use, the MEAs were sonicated in MiliQ water and carefully disassembled while fully submerged. This ensured maximum hydration and allowed for an intact separation of the anode from the membrane for subsequent analysis of both components.

Results Summary and Discussion 4

4.1 Paper I: fuel cell gas diffusion layers 23
4.2 Paper II: carbon nanofiber electrolyzer anodes 25

This thesis is based on the results of two papers, each of which uses identical location microscopy methods to look at different structures in PEM devices. Paper I focuses on the gas diffusion layer (GDL) in fuel cells, using Raman mapping co-located with SEM and EDX imaging to evaluate the distribution of PTFE in two different GDL microstructures. Paper II focuses on a novel porous transport electrode (PTE) for electrolyzers based on platinum-sheathed carbon nanofibers, which offer a high surface area in the immediate near-membrane region and are sufficiently robust to survive extensive testing and mechanical cell disassembly intact.

4.1 Paper I: fuel cell gas diffusion layers

Paper I combined confocal Raman microscopy with SEM-EDX imaging to track the spatial distribution of different loadings of polytetrafluoroethylene (PTFE) within two types gas diffusion layer (GDL) microstructures. The GDL types in question were a dense carbon fiber felt without a native binder (the F-H23 GDL) and a more porous GDL consisting of straighter, thinner carbon fibers held together by a binder (the SGL-39AA GDL). Part of the novelty of the work came from the direct comparison of the techniques involved. While EDX relies on tracking elemental fluorine, Raman spectroscopy identifies the vibrational signatures of the C-C and C-F bonds (see figure 4.1). Both techniques were able to distinguish PTFE. EDX imaging was significantly faster than Raman mapping and had a higher spatial resolution, but struggled to image PTFE when it was very dispersed. It also suffered from shadowing artifacts, as the detector was not in-line with the incident beam. If future materials move away from fluorinated polymers as a hydrophobic agent, Raman mapping, which relies on signature chemical bonds, may be required if elemental fluorine cannot be used as a marker for EDX.

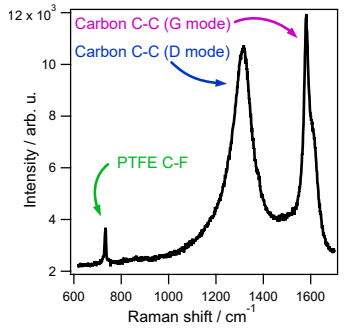

Figure 4.1: Typical spectrum from a Raman mapping experiment. The spectrum shows the D and G carbon C-C vibrational modes and the PTFE C-F stretching mode.

The two different GDL microstructures revealed fundamentally different PTFE agglomeration behaviors. In the binder-free, felt-like F-H23 GDL, PTFE accumulated preferentially at the junctions between the carbon fibers. In the SGL-39AA GDL, which contains a pre-existing binder and features straight, untangled fibers, the PTFE formed smaller, more dispersed agglomerates, primarily over the binder phase rather than on or in between fibers.

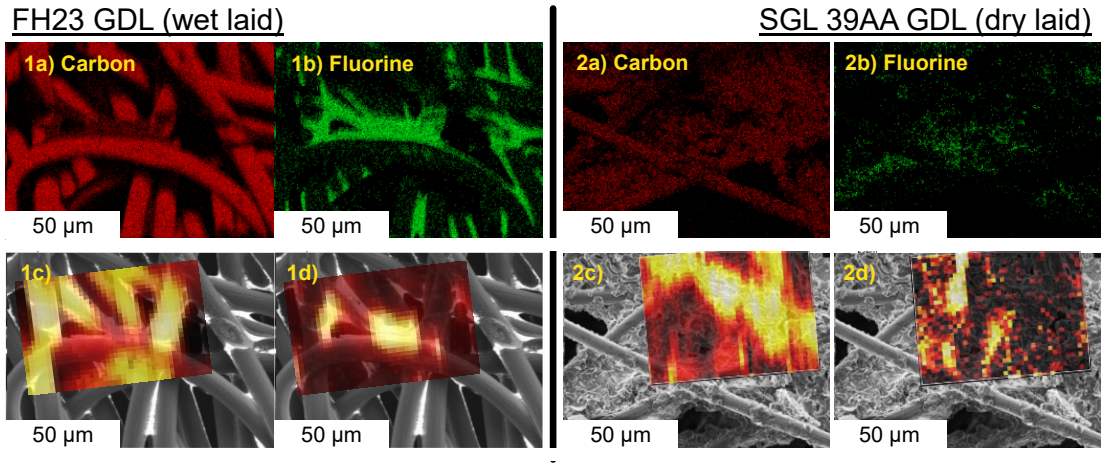

Figure 4.2: Identical location Raman mapping and SEM/EDX imaging of the wet-laid F-H23 (left) and dry-laid SGL-39AA (right) GDLs.

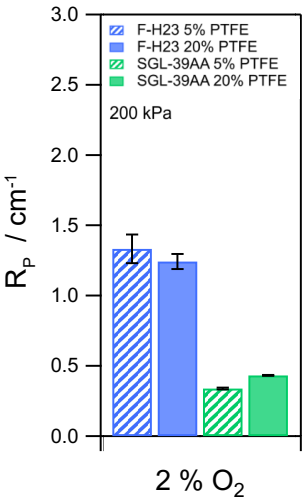

Figure 4.3: A representative bar graph for the pressure-dependent part of the (dry) oxygen transport resistance of each of the two GDL types, analyzed at at 200 kPa absolute pressure and 2 % O_2.

Cross-sectional mapping of the F-H23 GDL revealed that the PTFE agglomerates were distributed stochastically through the thickness of the material, rather than forming a concentration gradient weighted toward one surface. This may be a result of the ambient drying step on absorbent paper, as capillary action may have wicked the excess solvent away and prevented any gravity-driven pooling of the PTFE dispersion.

Finally, the study evaluated the *in-situ* electrochemical performance of these specific variations under dry operating conditions. The pressure-dependent oxygen transport resistance (see Figure 4.3) indicated that under dry conditions, the GDL microstructure is a significantly greater contributor to the mass transport resistance than the PTFE loading, though operations under humid conditions were not evaluated.

4.2 Paper II: carbon nanofiber electrolyzer anodes

Paper II focused on the oxygen-side electrode (anode) of the PEM electrolyzer, introducing a novel porous transport electrode architecture consisting of platinized carbon nanofibers. The aim was to drastically increase the active surface area in the immediate near-membrane region, thereby improving mass transport and, by localizing the catalyst in the most active part of the electrode, reducing the iridium loading of the electrode to below 0.2 mg cm^{-2}. A key challenge was that in order to engineer the immediate near-catalyst region, the nanofiber structure needs to remain chemically and structurally intact through assembly, disassembly, and operation.

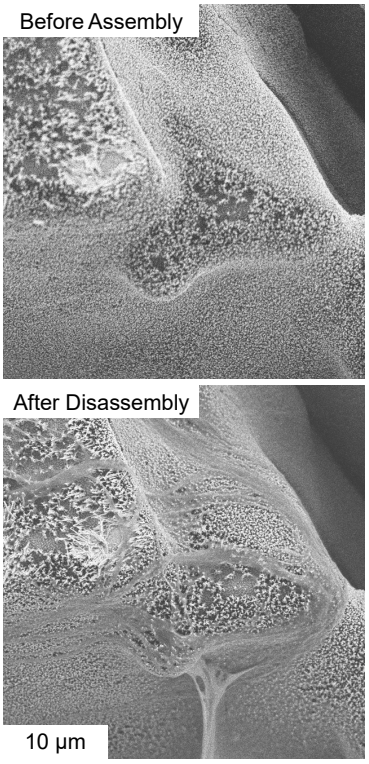

Figure 4.4: Identical location SEM imaging of a PTE section before assembly (top) and after disassembly (bottom).

As confirmed by identical location SEM imaging (see Figure 4.4), the nanofibers and their protective platinum sheathing remained intact following both MEA assembly and subsequent disassembly. Critically, the intact disassembly allowed for analysis of the membrane-facing side of the electrode, which is more involved in the electrochemical reactions. Separate SEM and TEM analysis on a PTE sample operated continuously over 1000 hours at 2 A/cm^2 confirmed the survivability of the nanofibers through extended operation. The conductivity of the anode did not degrade significantly, indicating that the titanium grains beneath the nanofibers were not passivated and that the platinum sheathing of the fibers also protected the titanium grains from oxidation.

Because the PTE is rigid and noncompliant, and the nanofibers on its surface remain intact after disassembly, distinct physical imprints of the PTE are left on the softer polymer membrane after MEA assembly and operation. Identifying both an imprint an its originating grain then allows the structure of both sides of the membrane-electrode interface to be studied, showing that nanofibers on sharper grain 'ridges' are at greater risk of detachment than ones on more even sections (see Figure 4.5). These imprints show that the active interfacial coverage is not completely uniform, with varying imprint depths caused by the grains, as well as non-imprinted areas (channels) between them. The imprinted region of the membrane represents the most active reaction zone, so the imprint coverage is important to understand the effective active area of the MEA. Incomplete imprint coverage of the membrane implies that the active regions operate at local current densities significantly higher than the nominal geometric area suggests. The influence of PTE grain size, morphology, and assembly parameters on the imprint coverage should therefore be examined in future work.

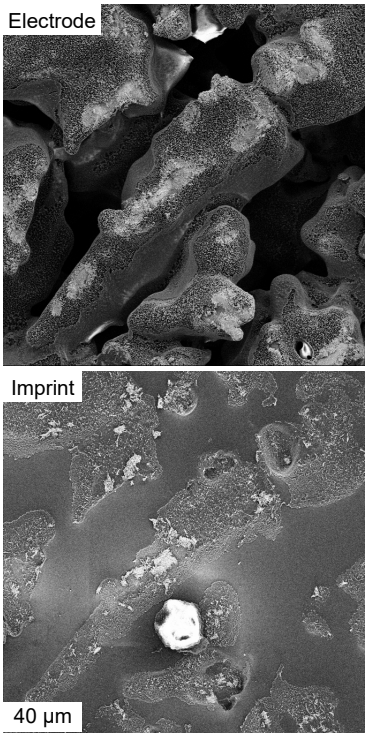

Figure 4.5: A PTE electrode grain (top) alongside its corresponding physical imprint left in the polymer membrane (bottom).

The impact of this localized contact on the membrane was investigated using confocal Raman microscopy. Spectra taken from the end-of-life membrane comparing the signatures of the imprints

to the adjacent channels showed a noticeably higher loss of the proton-conducting sulfonate ($-SO_3$) groups in the imprinted regions compared to the channels. Because the imprinted regions are in direct proximity to the anode, it is likely they carry the bulk of the proton conduction current. This might hasten functional group loss in these regions, though the increased surface area of the imprinted regions may be relevant as well[1].

1: A major source of functional group loss is the formation of H_2O_2 on the oxygen-electrode following hydrogen crossover, which can then form aggressive oxygen-radical species [62]. This mechanism is indeed expected to cause functional group loss disproportionately on the imprinted regions of the membrane, as that is where the electrode and membrane are in closest proximity.

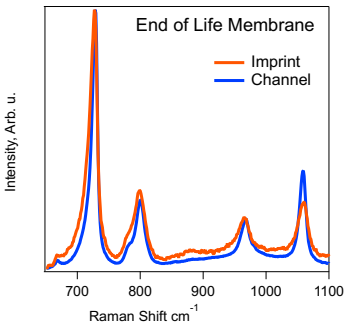

Figure 4.6: Raman spectra of the end-of-life membrane's imprinted and channel regions, normalized to the peak height of the C-F backbone signal.

While the CNF scaffold proved structurally resilient, the *operando* testing highlighted a major limitation regarding the active catalyst layer. Figure 4.7 displays the cell voltage over the 1000-hour durability test and shows an unexpected "S-curve": an initial potential of 2.1 V rapidly and exponentially increases before stabilizing at a plateau of approximately 2.53 V after just 10 hours. We cautiously attribute this behavior to the dissolution of the iridium oxide catalyst, which is believed to be in its less stable, amorphous state. Modern literature shows similar behavior on planar thin-film PTEs, though the timeline observed here is vastly accelerated—plateauing in 10 hours rather than the hundreds of hours reported elsewhere [63]. We attribute this acceleration to the CNF structure, which significantly increases the near-membrane surface area and thereby spreads the iridium catalyst more thinly. The voltage plateau at 2.53 V is poorly understood. We suggest that the underlying platinum layer may take on the catalytic role after the iridium dissolves, possibly with any remaining iridium alloyed to it, though a full mechanistic theory is beyond the scope of the present work.

While this work validates the structural viability of the CNF architecture, it also dictates a clear direction for future development: the inherently high surface area of the nanofibers must be paired with a highly stable OER catalyst, such as heat-treated rutile IrO_2, to prevent rapid dissolution and unlock the architecture's full performance potential.

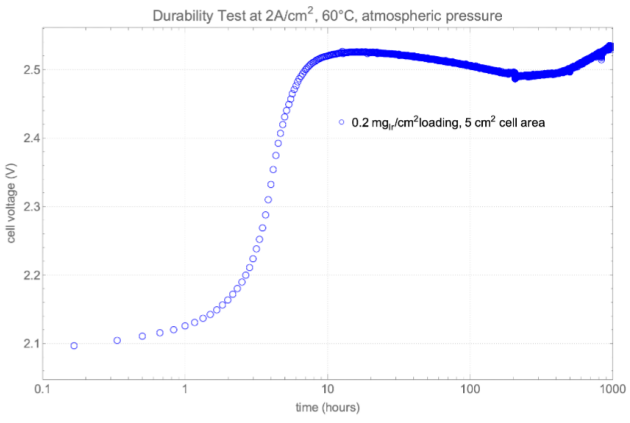

Figure 4.7: The *in-situ* durability test (2 A/cm^2, 60 °C, atmospheric pressure) utilizing a 0.2 mg$_{Ir}$/cm^2 catalyst loading on a 5 cm^2 cell area.

5 Conclusions

PEM devices, both fuel cells and electrolyzers, are both fascinating and difficult to study because of the complexity of the multi-phase components and transport processes which must coordinate on a micrometer scale. This thesis focuses on developing and applying identical location (IL) methods to couple structural and chemical characterization, particularly SEM-EDX and confocal Raman microscopy, in order to understand the structure, function and interface between different components in PEM fuel cells and electrolyzers.

In Paper I, which studied fuel cell gas diffusion layers, the base carbon architecture was shown to substantially dictate the distribution of the PTFE hydrophobic agent. In the case of a binder-free carbon fiber felt GDL, the polymer accumulated at fiber junctions. In the case of a GDL consisting of straight fibers held together with a binder, more disperse agglomerates formed on the binder phase instead. The work also showed the complementarity of Raman mapping with SEM and EDX when analyzing the the polymer distribution in GDL microstructures.

In Paper II, which studied a novel porous transport electrode for electrolyzers using platinum-sheathed carbon nanofibers, identical location imaging verified the structural survivability of the nanofiber architecture during assembly, disassembly and extended operation. The rigid and survivable nanofiber PTE was shown to leave non-uniform imprints on the membrane, which could be traced back to the originating imprint enabling a direct comparison of the structure on both sides of the electrode-membrane interface. Localized Raman spectroscopy showed a disproportionate loss of proton-conducting sulfonate ($-SO_3$) groups in the imprinted regions compared to the surrounding channel. The coverage of the imprinted region on the membrane was also studied, as it implies that the effective local current density may be higher than the geometric area would imply.

The greatest challenge to the carbon nanofiber electrode was shown to be the presently used catalyst, which *operando* testing indicated was subject to rapid degradation followed by stabilization. This unusual behavior was cautiously attributed to amorphous iridium oxide catalyst dissolving, and its function then shifting to the platinum sheath, with the rapid onset of dissolution credited to the high near-membrane surface area of the electrode. Ultimately, this work concludes that a nanofiber approach to engineering the membrane-electrode interface is promising, but currently incomplete, with the most pressing requirement being a sufficiently stable OER catalyst.

The path to durable, high-performance PEM devices requires mastering the micro-scale interaction of materials in the device layers and in the interfaces between components. It is through this precise, localized understanding that future PEM devices can be deliberately engineered to deliver peak performance.

5.1 Ideas for future work

In this section, I wish to discuss some ideas for future work in the second half of my PhD. The following is a non-exhaustive list of possible directions for future work, noting that I do not expect to be able to pursue every idea.

One of the conclusions from paper II was the need for a more stable iridium catalyst. At present, the catalyst is applied via electroplating and electrochemical oxidation, which is understood to result in a largely amorphous form of iridium oxide. The rutile form of iridium oxide is more electrochemically stable than the amorphous form, therefore a clear avenue of exploration is converting the amorphous iridium oxide to rutile. This should be achievable through thermal treatment, either in air or, after electrochemical oxidation, under inert atmosphere. Studying the performance of the carbon nanofiber anode architecture with a heat treated, rutile iridium oxide catalyst is of very great interest.

Paper II also showed the formation of imprints from the electrode left on the membrane, which notably do not cover the whole membrane area. Understanding the impact of different titanium grain substrates on the imprint behavior is another promising avenue of exploration. To this end, it should be sufficient to examine imprints after hot pressing bare titanium grain substrates without carbon nanofibers. That would allow for a much more rapid examination of the imprint behavior of different substrates. MEA assembly should be varied for conditions such as the pressure and time of the hot pressing step. Substrates for such a project should be chosen with different grain sizes and porosities, and the imprints examined for depth and degree of coverage.

Finally, a more ambitious project idea concerns the nature of the three-phase boundary and the underexplored phenomenon of ionomer poisoning of platinum group metal catalysts. Ionomers like Nafion provide reliable proton conduction, but are also known to adsorb onto and poison catalyst surfaces. I want to decouple the impact of ionomer conduction from ionomer poisoning by developing model electrodes featuring nanowells to simulate pores of various sizes. Because ionomers are physically excluded from sufficiently narrow pore structures, I hope to use lithographic methods to create nanowells where the center is ionomer-coated while the narrow edges remain ionomer-free. By varying the diameter of the nanowells, I hope to vary the ratio of ionomer-covered

'center' to ionomer-excluded 'edge' in the nanowells. Subsequent electrochemical testing could isolate ionomer-specific transport resistances and poisoning mechanisms, ultimately providing a much clearer picture of how the three-phase boundary functions and what the activity of the catalyst is when in direct contact with ionomer compared to simply close proximity to the ionomer.

5.2 Closing thoughts and the future of hydrogen

The most important challenge I see in the near term for the hydrogen industry is not the creation of a complex electricity balancing system using hydrogen as a storage medium, but rather the decarbonization of the hydrogen we already use. As discussed in the introduction, there is a significant global demand already for hydrogen, which comes from vital industries like ammonia production, and that demand is currently met by producing hydrogen from fossil sources. As long as this is the case, fuel cells are not a renewable technology, they are just fossil fuels with extra steps. The near term challenge for the hydrogen industry should focus on the rapid, large-scale expansion of electrolyzers.

On a purely technical level, PEM electrolyzers are viable. So where is the investment? When I have talked at conferences to people from industrial electrolyzer providers, variable costs, like the cost of the noble metal catalysts which are always the same no matter how many electrolyzers you produce, are not considered the primary challenge. Fixed costs are. Economically, the returns of an electrolyzer must be balanced against the capital expenditures and operating expenditures involved. Here, there is potential. Renewables are now much cheaper than fossil fuel sourced energy, and this will make electricity much more available and much cheaper globally. Therefore, the operating expenditures should decrease. The capital expenditures are dependent on economies of scale. The more electrolyzer demand there is, the more of them are built, the more fixed costs such as research and equipment come down, and the cheaper many of the components become. This means the initial hurdle for electrolyzers to be produced on a large scale might come down if the demand is there. We have seen this happen before with technologies like lithium-ion batteries, which have become much cheaper despite the price of lithium increasing significantly.

There is a potential new source for this demand as well. By now it is obvious that green energy arguments for building hydrogen infrastructure have been insufficient. Now, we see new arguments based on security and sovereignty motivate enormous amounts of investment. This might benefit the hydrogen industry as hydrogen promises to be a vastly scalable energy storage solution that could help with energy security. Additionally, nitrogen fixation via the Haber-Bosch process is vital for the production of fertilizers, as well

as explosives. It could therefore be considered sufficiently critical for on-shoring or near-shoring, and the Haber-Bosch process requires hydrogen which can be delivered by electrolysis. Only time will tell whether any of this potential is actually reached.

I want to close this thesis with a concern I have regarding the field of electrolysis. The case for producing clean hydrogen is, I think, very strong. This is not true for the produced oxygen though. Oxygen is not required in the same quantities as hydrogen and offers only a fraction of the value. Despite this, much of the research in electrolysis is going to the oxygen reaction and the oxygen electrode. What if this is the wrong reaction? There are other anode chemistries, such as SO_2-depolarized electrolysis[1], in which the anodic reaction is used to drive the synthesis of a more valuable chemical product (in this case H_2SO_4). Because of the additional revenue stream, which can be higher in value than the produced hydrogen, such electrosynthesis devices might be more commercially viable than simply using the OER reaction at the anode. Fortunately, electrolyzers which do this kind of electrosynthesis have a very similar design and similar materials to conventional PEM electrolyzers, so at least some of the research should be mutually compatible. Even so, the main thrust of current electrolyzer research may be optimizing for the wrong reactions.

1: $SO_2 + 2\,H_2O \rightleftharpoons H_2SO_4 + H_2$

Bibliography

(1) D. Schulz, M. Ringström, S. Sankar and A. Martinelli, 'The Role of Native Binder in Controlling the Polytetrafluoroethylene Distribution in Gas Diffusion Layers for Proton Exchange Membrane Fuel Cells', Accepted in Fuel Cells, 2026 (cit. on p. vii).

(2) D. Schulz, X. Wen, B. Penninckx, S. Sasidharan, L. Strandberg, F. Wenger and A. Martinelli, 'Robust anodes for PEM electrolysers based on platinized carbon nanofibers with low iridium loading', In manuscript (cit. on p. vii).

(3) Our World in Data, *Life expectancy (years) dataset*, Data compiled from UN WPP, Human Mortality Database, Zijdeman et al. (2015), and Riley (2005). Accessed: 2026-06-04, 2023 (cit. on p. 1).

(4) United Nations, Department of Economic and Social Affairs, Population Division, *World Population Prospects 2024: Summary of Results*, tech. rep. UN DESA/POP/2024/TR/NO. 1, United Nations, 2024 (cit. on p. 1).

(5) A. Bilal and D. R. Känzig, *The Macroeconomic Impact of Climate Change: Global vs. Local Temperature*, Working Paper 32450, National Bureau of Economic Research, 2024 (cit. on p. 1).

(6) United Nations Environment Programme, *Annual Report 2025: Our planet. Our purpose. The way forward is together*, tech. rep., United Nations Environment Programme, Nairobi, Kenya, 2026 (cit. on p. 1).

(7) M. J. Albert, *Review of International Political Economy*, 2021, **29**, 1766–1781 (cit. on p. 1).

(8) R. Mori, *RSC Sustainability*, 2023, **1**, 179–212 (cit. on p. 1).

(9) International Energy Agency, *Net Zero Roadmap: A Global Pathway to Keep the 1.5 °C Goal in Reach*, tech. rep., IEA, Paris, France, 2023 (cit. on p. 1).

(10) International Energy Agency, *Electricity 2026: Analysis and forecast to 2030*, tech. rep., International Energy Agency, Paris, France, 2026 (cit. on pp. 1, 4).

(11) Our World in Data, *Levelized cost of energy*, https://ourworldindata.org/grapher/levelized-cost-of-energy, Based on data from the International Renewable Energy Agency (IRENA). Accessed: 2026-06-25, 2023 (cit. on p. 1).

(12) International Renewable Energy Agency, *Renewable Power Generation Costs in 2023*, tech. rep., IRENA, Abu Dhabi, United Arab Emirates, 2024 (cit. on pp. 1, 4).

(13) P. Breeze, *Power System Energy Storage Technologies*, Academic Press, 2018 (cit. on p. 1).

(14) International Energy Agency, *Global Hydrogen Review 2025*, tech. rep., International Energy Agency, Paris, France, 2025 (cit. on pp. 2, 4).

(15) M. Ball and M. Wietschel, *The Hydrogen Economy: Opportunities and Challenges*, Cambridge University Press, Cambridge, UK, 2009 (cit. on p. 2).

(16) W. Vielstich, A. Lamm and H. A. Gasteiger, *Handbook of Fuel Cells: Fundamentals, Technology, and Applications*, John Wiley & Sons, Chichester, England, 2003 (cit. on pp. 2, 5, 7–10, 19).

(17) T. D. Crouch, *The Eagle Aloft: Two Centuries of the Balloon in America*, Smithsonian Institution Press, Washington, DC, 1983 (cit. on p. 3).

(18) J. M. Modak, *Resonance*, 2011, **16**, 1159–1167 (cit. on p. 3).

(19) A. C. Ching, A. P. Gillis and F. M. Plauche, *Fuel cell powerplant operation in Apollo spacecraft*, tech. rep. NASA-TM-X-67652, National Aeronautics and Space Administration, 1972 (cit. on p. 3).

(20) A. R. Nerheim, V. Æsøy and F. T. Holmeset, *Journal of Marine Science and Engineering*, 2021, **9**, 743 (cit. on p. 3).

(21) U.S. Department of Energy, *Hydrogen Storage*, https://www.energy.gov/cmei/fuels/hydrogen-storage, Accessed: 2026-06-12, 2026 (cit. on p. 3).

(22) International Energy Agency, *Integrating Solar and Wind: Global experience and emerging challenges*, tech. rep., International Energy Agency, Paris, France, 2024 (cit. on p. 3).

(23) European Network of Transmission System Operators for Electricity (ENTSO-E), *Transparency Platform: Actual Generation per Production Type and Actual Total Load [SE3 Bidding Zone]*, https://transparency.entsoe.eu/, Data retrieved for the period 2026-06-15 to 2026-06-21. Accessed: 2026-06-26, 2026 (cit. on p. 4).

(24) International Energy Agency, *The Future of Hydrogen: Seizing today's opportunities*, tech. rep., International Energy Agency, Paris, France, 2019 (cit. on p. 4).

(25) J. R. Rostrup-Nielsen, in *Catalysis: Science and Technology*, ed. J. R. Anderson and M. Boudart, Springer-Verlag, 1984, vol. 5, pp. 1–117 (cit. on p. 4).

(26) A. Chugh and E. Taibi, *What is green hydrogen and why do we need it?*, https://www.weforum.org/stories/2021/07/clean-energy-green-hydrogen/, Accessed: 2026-06-12, 2021 (cit. on p. 4).

(27) N. A. Qasem and G. A. Abdulrahman, *International Journal of Energy Research*, 2024, **2024**, 7271748 (cit. on p. 5).

(28) R. O'Hayre, S.-W. Cha, W. Colella and F. B. Prinz, *Fuel Cell Fundamentals*, John Wiley & Sons, 3rd, 2016 (cit. on pp. 5, 11–13).

(29) M. Chatenet, B. G. Pollet, D. R. Dekel, F. Dionigi, J. Deseure, P. Millet, R. J. Braatz, M. Z. Bazant, M. Eikerling, I. Staffell, P. Balcombe, Y. Shao-Horn and H. Schäfer, *Chemical Society Reviews*, 2022, **51**, 4583–4762 (cit. on pp. 5, 7–13, 20).

(30) M. Carmo, D. L. Fritz, J. Mergel and D. Stolten, *International Journal of Hydrogen Energy*, 2013, **38**, 4901–4934 (cit. on pp. 5, 12).

(31) J. Rossmeisl, Z.-W. Qu, H. Zhu, G.-J. Kroes and J. K. Nørskov, *Journal of Electroanalytical Chemistry*, 2005, **607**, 83–89 (cit. on pp. 7, 8).

(32) K. S. Exner, *ChemCatChem*, 2021, **13**, 4066–4074 (cit. on p. 8).

(33) J. K. Nørskov, J. Rossmeisl, A. Logadottir, L. Lindqvist, J. R. Kitchin, T. Bligaard and H. Jónsson, *The Journal of Physical Chemistry B*, 2004, **108**, 17886–17892 (cit. on pp. 8, 9).

(34) I. C. Man, H.-Y. Su, F. Calle-Vallejo, H. A. Hansen, J. I. Martínez, N. G. Inoglu, J. Kitchin, T. F. Jaramillo, J. K. Nørskov and J. Rossmeisl, *ChemCatChem*, 2011, **3**, 1159–1165 (cit. on p. 9).

(35) A. Kusoglu and A. Z. Weber, *Chemical Reviews*, 2017, **117**, 987–1104 (cit. on p. 10).

(36) P. A. García-Salaberri, *Sustainable Materials and Technologies*, 2023, **38**, e00727 (cit. on p. 10).

(37) W. Y. Hsu and T. D. Gierke, *Journal of Membrane Science*, 1983, **13**, 307–326 (cit. on p. 10).

(38) D. A. Cullen, R. Koestner, R. S. Ahluwalia et al., *Nature Energy*, 2021, **6**, 462–474 (cit. on pp. 10, 11).

(39) J. K. Lee, G. Anderson, A. W. Tricker, F. Babbe, A. Madan, D. A. Cullen, J. D. Arregui-Mena, N. Danilovic et al., *Nature Communications*, 2023, **14**, 4592 (cit. on p. 11).

(40) Z. Fishman and A. Bazylak, *Journal of The Electrochemical Society*, 2011, **158**, B841 (cit. on pp. 11, 12).

(41) H. Ito, K. Abe, M. Ishida, A. Nakano, T. Maeda, T. Munakata, H. Nakajima and T. Kitahara, *Journal of Power Sources*, 2014, **248**, 822–830 (cit. on p. 12).

(42) Y. Song, C. Zhang, C.-Y. Ling, M. Han, R.-Y. Yong, D. Sun and J. Chen, *International Journal of Hydrogen Energy*, 2020, **45**, 29832–29847 (cit. on p. 12).

(43) W. Tang, S. Wang, S. Li, S. Yu, X. Yuan, C. Yang and W. Li, *Next Materials*, 2024, **4**, 100062 (cit. on p. 12).

(44) M. Langemann, D. L. Fritz, M. Müller and D. Stolten, *International Journal of Hydrogen Energy*, 2015, **40**, 11385–11391 (cit. on p. 12).

(45) International Renewable Energy Agency, *Green Hydrogen Cost Reduction: Scaling up Electrolysers to Meet the 1.5°C Climate Goal*, tech. rep., IRENA, Abu Dhabi, 2020 (cit. on p. 13).

(46) H. Wang and Y. Fan, *Engineering*, 2018, **4**, 352–360 (cit. on p. 13).

(47) M. Yue et al., *Energy Conversion and Management: X*, 2026, **30**, 101866 (cit. on pp. 13, 14).

(48) E. Weidner, F. Dolci, A. Georgakaki, S. Letout, A. Mountraki, E. Ince, D. Shtjefni, M. Wegener, J. Gea Bermudez, M. Jaxa-Rozen, R. Salvucci, F. Neuwahl, P. Sikora, M. Rózsai, A. Schmitz, B. Schade, K. Keramidas and F. Fosse, *Clean Energy Technology Observatory: Fuel Cell Technology in the European Union - 2025 Status Report on Technology Development, Trends, Value Chains and Markets*, tech. rep. JRC144322, Joint Research Centre (JRC), European Commission, Luxembourg, 2025 (cit. on p. 14).

(49) J. M. Hollas, *Modern Spectroscopy*, John Wiley & Sons, Chichester, UK, 4th, 2004 (cit. on p. 15).

(50) J. I. Goldstein, D. E. Newbury, J. R. Michael, N. W. Ritchie, J. H. Scott and D. C. Joy, *Scanning Electron Microscopy and X-Ray Microanalysis*, Springer, New York, NY, 4th, 2017 (cit. on pp. 16, 17).

(51) D. B. Williams and C. B. Carter, *Transmission Electron Microscopy: A Textbook for Materials Science*, Springer, New York, NY, 2nd, 2009 (cit. on pp. 16, 17).

(52) Thermo Fisher Scientific, *SEM: Types of Electrons and the Information They Provide*, https://www.thermofisher.com/blog/materials/sem-signal-types-electrons-and-the-information-they-provide/, Accessed: 2026-07-01, n.d. (Cit. on p. 16).

(53) P. Baatsen, S. Gabarre, K. Vints, R. Wouters, D. Vandael, R. Goodchild, S. Munck and N. V. Gounko, *Frontiers in Cell and Developmental Biology*, 2021, **9**, 737621 (cit. on p. 17).

(54) L. A. Giannuzzi and F. A. Stevie, *Introduction to Focused Ion Beams: Instrumentation, Theory, Techniques and Practice*, Springer, New York, NY, 2005 (cit. on p. 17).

(55) L. Strandberg, Licentiate thesis, Chalmers University of Technology, Gothenburg, Sweden, 2023 (cit. on p. 18).

(56) D. Pletcher, *A First Course in Electrode Processes*, Royal Society of Chemistry, Cambridge, UK, 2nd, 2009 (cit. on pp. 19, 20).

(57) D. R. Baker, C. Wieser, K. C. Neyerlin and M. W. Murphy, *Ecs Transactions*, 2006, **3**, 989 (cit. on p. 19).

(58) S. Brunauer, P. H. Emmett and E. Teller, *Journal of the American Chemical Society*, 1938, **60**, 309–319 (cit. on p. 21).

(59) G. Calleja, A. Jourdan, B. Ameduri and J.-P. Habas, *European Polymer Journal*, 2013, **49**, 2214–2222 (cit. on p. 22).

(60) A. N. Garcia, N. Viciano and R. Font, *Journal of Analytical and Applied Pyrolysis*, 2007, **80**, 85–91 (cit. on p. 22).

(61) V. Desmaris, M. A. Saleem and S. Shafiee, *IEEE Nanotechnology Magazine*, 2015, **9**, 33–38 (cit. on p. 22).

(62) F. C. Teixeira, A. P. S. Teixeira and C. M. Rangel, *International Journal of Hydrogen Energy*, 2023, **48**, 37489–37499 (cit. on p. 26).

(63) J. L. Young, D. E. Beltrán, S. J. Blair, R. P. M. Duarte, M. R. Parimuha, H. Yu, L. van Eijk, K. S. Reeves, T. Grejtak, J. Martinez, B. A. Chao, J. Wrubel, M. E. Kreider, E. M. Miller, J. D. Lenef, K. N. Heinselman, S. Pylypenko, D. A. Cullen and G. Bender, *Advanced Science*, 2026, **13**, e17655 (cit. on p. 26).